

Spectroscopy in the $Z=49$ ^{108,110}In isotopes: Lifetime measurements in shears bands

C. J. Chiara,^{1,*} D. B. Fossan,¹ V. P. Janzen,² T. Koike,¹ D. R. LaFosse,¹ G. J. Lane,^{1,†} S. M. Mullins,^{3,‡} E. S. Paul,⁴ D. C. Radford,^{2,§} H. Schnare,¹ J. M. Sears,¹ J. F. Smith,^{1,||} K. Starosta,¹ P. Vaska,^{1,¶} R. Wadsworth,⁵ D. Ward,^{2,**} and S. Frauendorf^{6,7}

¹Department of Physics and Astronomy, State University of New York at Stony Brook, Stony Brook, New York 11794-3800

²AECL Research, Chalk River Laboratories, Chalk River, Ontario, Canada K0J 1J0

³Department of Physics and Astronomy, McMaster University, Hamilton, Ontario, Canada L8S 4M1

⁴Oliver Lodge Laboratory, University of Liverpool, Liverpool L69 7ZE, United Kingdom

⁵Department of Physics, University of York, Heslington, York YO1 5DD, United Kingdom

⁶Department of Physics, University of Notre Dame, Indiana 46556

⁷Institut für Kern- und Hadronenphysik, Forschungszentrum Rossendorf, PF 510119, D01314 Dresden, Germany

(Received 22 March 2001; published 18 October 2001)

Excited states have been populated in ¹⁰⁸In and ¹¹⁰In in complementary backed- and thin-target experiments using the Stony Brook and the 8 π Ge-detector arrays. The level schemes for both isotopes have been extended and modified, including the first observation of $\Delta I=2$ bands in ¹¹⁰In. Lifetimes of states in four $\Delta I=1$ bands and one $\Delta I=2$ band have been measured using the Doppler-shift attenuation method. Experimental total angular momenta and reduced transition strengths for the $\Delta I=1$ bands have been compared with tilted axis cranking predictions for shears bands with configurations involving one proton $g_{9/2}$ hole and one or three valence quasineutrons from the $h_{11/2}$ and $g_{7/2}/d_{5/2}$ orbitals. The $\Delta I=2$ bands have been compared with principal axis cranking predictions for configurations with two $g_{9/2}$ proton holes and a $g_{7/2}$ or $d_{5/2}$ proton and one- or three-quasineutron configurations involving the $h_{11/2}$ and $g_{7/2}/d_{5/2}$ orbitals. In general, there is good overall agreement for both the angular momenta and reduced transition strengths. The $\Delta I=1$ and $\Delta I=2$ bands have large $\mathcal{J}^{(2)}/B(E2)$ ratios as expected for the shears mechanism. The $B(M1)$ strengths deduced for the $\Delta I=1$ bands show a decreasing trend as a function of spin, which is also a feature of the shears mechanism. Configuration assignments have been made for most observed bands based on comparisons with theory and systematics of neighboring nuclei.

DOI: 10.1103/PhysRevC.64.054314

PACS number(s): 23.20.Lv, 21.10.Tg, 27.60.+j, 25.70.Gh

I. INTRODUCTION

Nuclei in the $A\sim 110$ region have been studied in recent years in search of bands exhibiting properties characteristic of the shears mechanism, a prediction of tilted axis cranking (TAC) [1]. In such bands, angular momentum is generated in a manner that appears similar to collective rotation in well-deformed nuclei, despite the small deformations of these nuclei in the proximity of the $Z=50$ spherical shell gap. Evidence of this phenomenon has been reported in the neutron-deficient ⁴⁸Cd [2–4], ⁵⁰Sn [5,6], and ⁵¹Sb [7] nuclei, which have $\Delta I=1$ bands based on high- Ω $g_{9/2}$ proton holes and low- Ω $g_{7/2}/d_{5/2}$ and $h_{11/2}$ neutrons. Similar bands are ex-

pected in the ⁴⁹In isotopes and have already been reported in the odd- A isotopes ^{107,109,111,113}In [8,9]; two of the bands in ¹¹¹In and ¹¹³In have been suggested to be shears bands [9,10].

The successful interpretation of these $\Delta I=1$ bands suggests that further exploration in this mass region is worthwhile in order to extend the experimental information for odd-odd nuclei which have configurations of valence nucleons that are favorable for the shears mechanism. Furthermore, nuclei with $Z<50$ and $N>50$ are also predicted to possibly develop $\Delta I=2$ shears bands; this phenomenon was first reported in ¹⁰⁹Cd [2] and is discussed in Ref. [11] for ¹¹⁰Cd. The odd-odd In isotopes should, hence, be good candidates in which to study both forms of shears bands.

Figure 1(a) illustrates the shears mechanism for a $\Delta I=1$ band, known as magnetic rotation. The component μ_{\perp} of the magnetic dipole moment perpendicular to the total spin \mathbf{I} is large at the bandhead and decreases as the valence proton-hole \mathbf{j}_{π} and neutron-particle \mathbf{j}_{ν} spin vectors align. Since the $B(M1)$ reduced magnetic dipole transition strength is proportional to μ_{\perp}^2 , magnetic-rotational bands are predicted to exhibit a pronounced decrease in $B(M1)$ strength with increasing spin, a feature which can distinguish them from bands which maintain a fixed projection K of the angular momentum on the symmetry axis [12]. (A more detailed description of this mechanism can be found in Ref. [11].) Figure 1(b) illustrates the shears mechanism for a $\Delta I=2$ band, known as antimagnetic rotation. As these bands exist in mod-

*Present address: Department of Chemistry, Washington University, St. Louis, Missouri 63130.

†Present address: Department of Nuclear Physics, Australian National University, Canberra ACT 0200, Australia.

‡Present address: National Accelerator Center, P.O. Box 72, Faure 7131, South Africa.

§Present address: Bldg. 6000, M. S. 6371, Oak Ridge National Laboratory, P.O. Box 2008, Oak Ridge, Tennessee 37831-6371.

||Present address: Schuster Laboratory, University of Manchester, Manchester M13 9PL, United Kingdom.

¶Present address: Medical Department, Brookhaven National Laboratory, Upton, New York 11973.

**Present address: Nuclear Science Division, Lawrence Berkeley National Laboratory, Berkeley, California 94720.

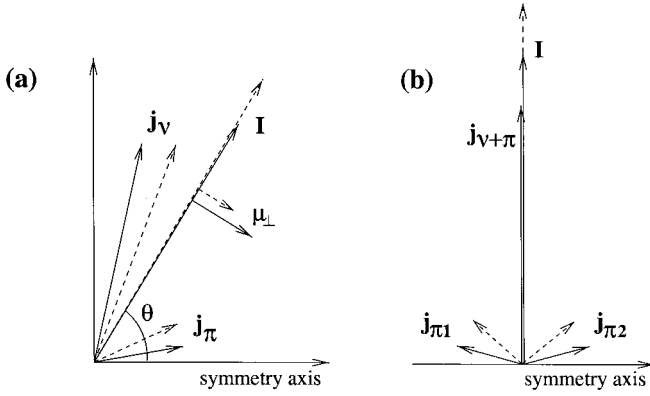


FIG. 1. (a) Illustration of the shears mechanism for a $\Delta I=1$ shears band (magnetic rotation) in the $A \sim 110$ region. The spin contributions from the proton hole \mathbf{j}_π and neutron particles \mathbf{j}_ν , and their corresponding vector sums \mathbf{I} , are shown at low (solid lines) and high (dashed lines) frequencies. Also shown are the components of the magnetic dipole moment perpendicular to \mathbf{I} . (b) Illustration of the shears mechanism for a $\Delta I=2$ shears band (antimagnetic rotation). The spin contributions from the two high- Ω proton holes are represented by $\mathbf{j}_{\pi 1,2}$; the contributions from the neutrons and the low- Ω proton particle are combined as $\mathbf{j}_{\nu+\pi}$. Solid and dashed lines are for low and high rotational frequencies, respectively.

estly deformed nuclei, the $B(E2)$ strength is expected to be small (for both types of shears bands). Furthermore, as the shears blades close and the rotational symmetry of the nucleus around the cranking axis is restored, the $B(E2)$ strength should decrease with increasing spin.

Measurements of the lifetimes of states in these bands can directly test the behavior of the reduced transition strengths predicted by the shears mechanism. Such measurements have confirmed the decreasing $B(M1)$ strength in shears bands in several cases in this mass region [2–4,13]. To date, the decrease in $B(E2)$ strength has yet to be experimentally established. Another criterion for associating a band with the shears mechanism is the ratio of the $\mathcal{J}^{(2)}$ dynamic moment of inertia to the $B(E2)$ strength. This ratio is predicted to be

over $100\hbar^2 \text{ MeV}^{-1} (e b)^{-2}$, an order of magnitude larger than the value for well-deformed rotational bands [11]. This is a consequence of the angular momentum originating from the closing shears blades, as opposed to a collective core. As noted in the review of the shears mechanism provided in Ref. [14], however, in the regime of weak pairing and small deformation this ratio may still be large (see, for example, Eq. 4–128 of Ref. [15]). Therefore, the large $\mathcal{J}^{(2)}/B(E2)$ ratio should perhaps be viewed as a necessary but not sufficient condition for the shears mechanism [16].

In this work, the level schemes of the isotopes $^{108,110}\text{In}$ have been significantly extended and several candidate magnetic-rotational (MR) and antimagnetic-rotational (AMR) shears bands have been observed. Lifetime measurements have been made for states in several of the bands. The systematic properties of these bands are discussed in the context of the shears interpretation. Configurations have been assigned to the majority of the observed bands based on theoretical predictions and systematic arguments.

II. EXPERIMENTAL DETAILS

The data described in this work were collected during a number of experiments which populated high-spin states in the odd-odd nuclei ^{108}In and ^{110}In . Both thin- and backed-target experiments were performed; thin-target experiments were performed so that the band structures of the two isotopes could be studied to high spins, and backed-target experiments were performed in order to measure short lifetimes (≤ 1 ps) of states via the Doppler-shift attenuation method (DSAM) [17]. The details of each experiment are provided in the following sections and are summarized in Table I.

A. Thin-target experiments

Excited states in ^{108}In were populated via the reaction $^{76}\text{Ge}(^{37}\text{Cl},5n)^{108}\text{In}$ (experiment 1 in Table I). A 138-MeV ^{37}Cl beam was provided by the Tandem Accelerator Superconducting Cyclotron (TASCC) facility at Chalk River Laboratories. Two stacked, self-supporting $300\text{-}\mu\text{g}/\text{cm}^2$ ^{76}Ge targets were used. The γ rays emitted in this reaction were detected

TABLE I. Experimental details. The Stony Brook (SB) array consisted of six Compton-suppressed Ge detectors and a 14-element BGO multiplicity (K) and sum-energy (H) filter; the 8π array consisted of 20 Compton-suppressed Ge detectors and a 71-element BGO ball.

	Laboratory	Reaction	Beam energy (MeV)	Target	Detector array	Trigger condition	Number of events ($\times 10^6$)
1	TASCC, Chalk River	$^{76}\text{Ge}(^{37}\text{Cl},5n)^{108}\text{In}$	138	$2 \times 300 \mu\text{g}/\text{cm}^2$ (stacked foils)	8π	$\gamma\gamma, K \geq 8$	88 ^a
2	TASCC, Chalk River	$^{96}\text{Zr}(^{19}\text{F},5n)^{110}\text{In}$	85	$500 \mu\text{g}/\text{cm}^2$	8π	$\gamma\gamma, K \geq 5$	54 ^a
3	NSL, Stony Brook	$^{94}\text{Mo}(^{18}\text{O},p3n)^{108}\text{In}$	85	$3 \text{ mg}/\text{cm}^2$ ^{94}Mo on $10.5 \text{ mg}/\text{cm}^2$ nat Pb	SB	$\gamma\gamma, K \geq 2$	150
4	NSL, Stony Brook	$^{96}\text{Zr}(^{19}\text{F},5n)^{110}\text{In}$	88	$2 \text{ mg}/\text{cm}^2$ ^{96}Zr on $15 \text{ mg}/\text{cm}^2$ ^{208}Pb	SB	$\gamma\gamma, K \geq 2$	203

^aIncludes off-line cut on H .

with the 8π array, which consisted of 20 Compton-suppressed, $\sim 25\%$ -efficient HPGe detectors and a 71-element inner BGO ball which served as a multiplicity (K) filter and sum-energy (H) calorimeter. Data were written to magnetic tape for events involving two or more unsuppressed γ rays detected by the Ge detectors in prompt time coincidence plus signals in at least eight elements of the BGO filter ($K \geq 8$). At the beam energy chosen for this experiment, the $4n$ evaporation channel leading to ^{109}In has the dominant cross section. By selecting only those events with $H < 15.4$ MeV, however, the ^{108}In reaction channel was enhanced over ^{109}In . A total of 88×10^6 events satisfying the trigger condition and the off-line cut on H were recorded during the run.

The isotope ^{110}In was populated in a thin-target experiment (labeled 2 in Table I) at Chalk River using the reaction $^{96}\text{Zr}(^{19}\text{F},5n)$. An 85-MeV ^{19}F beam was provided by the TASC facility and directed onto a $500\text{-}\mu\text{g}/\text{cm}^2$ self-supporting ^{96}Zr target. In addition to ^{110}In , the $4n$ evaporation channel leading to ^{111}In was also strongly populated in this reaction [8,9], but by placing a cut on $H < 13.4$ MeV, the $5n$ evaporation channel was enhanced. The 8π array was again used with the same detector configuration and trigger condition described for experiment 1, apart from the filter condition being reduced to $K \geq 5$. A total of 54×10^6 events satisfied the trigger condition and the off-line cut on H .

B. Backed-target experiments

Excited states in ^{108}In were populated in a complementary backed-target experiment using the reaction $^{94}\text{Mo}(^{18}\text{O},p3n)$ (experiment 3 in Table I). An 85-MeV ^{18}O beam was provided by the FN tandem/superconducting linac facility at the Stony Brook Nuclear Structure Laboratory (NSL). An excitation function performed at Stony Brook determined that 85 MeV was the optimal beam energy for producing ^{108}In in this reaction. The ^{108}In yield was about 20% of the total fusion cross section for this reaction, an approximately 5% improvement over experiment 1. More significantly, in experiment 3, ^{108}In is about 35% stronger than the next strongest channel ^{108}Cd ($2p2n$ evaporation channel), whereas in experiment 1, ^{108}Cd ($p4n$) is produced with 80% more intensity than ^{108}In , and ^{106}Ag ($\alpha 3n$) and ^{108}In are produced with approximately equal intensity.

The target consisted of $3\text{ mg}/\text{cm}^2$ of ^{94}Mo backed with $10.5\text{ mg}/\text{cm}^2$ of natural Pb. This target thickness was determined to provide sufficient stopping power to slow down and stop the recoiling reaction products and to allow DSAM lifetime measurements to be performed. The average recoil velocity for this reaction ($\beta \approx 1.6\%$) is smaller than the recoil velocity for the $^{76}\text{Ge}(^{37}\text{Cl},5n)$ reaction ($\beta \approx 2.9\%$), but the disadvantage of having smaller Doppler shifts is compensated by the increased cross section.

Excited states in ^{110}In were also populated in a complementary backed-target experiment (4 in Table I), using the same reaction as for experiment 2. An 88-MeV ^{19}F beam, the beam energy determined by an excitation function to produce the maximum ^{110}In yield in this reaction, was provided by the Stony Brook accelerator facility. The beam was directed

onto a $2\text{-mg}/\text{cm}^2$ ^{96}Zr target backed with $15\text{ mg}/\text{cm}^2$ of ^{208}Pb , producing recoils with an average $\beta \approx 1.6\%$ velocity.

The Stony Brook array of six Compton-suppressed, $\sim 25\%$ -efficient HPGe detectors was used to detect the γ rays emitted in both experiments 3 and 4. The detectors were placed in a planar arrangement, two at forward angles (26° , 25° relative to the beam direction), two at $\sim 90^\circ$ (80° , 91°), and two at backward angles (144° , 142°). A 14-element BGO multiplicity filter covering $\sim 80\%$ of the total solid angle was used in the trigger condition for valid events. Data were written to tape only for events which involved at least two γ rays in prompt time coincidence in the Ge detectors and satisfied a multiplicity condition of $K \geq 2$. A total of 150×10^6 and 203×10^6 γ - γ events were written to tape for experiments 3 and 4, respectively.

III. ANALYSIS METHODS

The data from the thin-target experiments were sorted off line into symmetrized E_γ - E_γ coincidence matrices. The RADWARE program ESCL8R [18] was used to project background-subtracted gated spectra from the matrices. Use of a thin target and application of a Doppler correction to γ -ray energies provided sensitivity to fast transitions originating from high-spin states. Coincidence relationships extracted from the gated spectra allowed level schemes for ^{108}In and ^{110}In to be constructed, the details of which are discussed in Secs. IV A and IV B.

The data from the backed-target experiments were sorted off line in three ways, as explained below.

(i) Symmetrized E_γ - E_γ coincidence matrices were created and analyzed using ESCL8R, as above. For the ^{110}In matrix, the $5n$ channel was enhanced over the $4n$ channel to ^{111}In by selecting off line only those events which had an associated multiplicity of $K \leq 7$. In addition, the background in this matrix was reduced by placing a time gate on events occurring promptly following linac beam bursts. The choice of a relatively light beam in both experiments resulted in enhanced population of nonyrast states up to moderate spins. This enabled the observation of transitions feeding out of low- and moderate-spin states that were not strongly populated in the thin-target experiments.

(ii) Asymmetric angular correlation matrices were sorted in order to measure directional correlations from oriented states (DCO ratios) [19]. These matrices were sorted with γ rays detected in the two detectors at $\theta \sim 90^\circ$ on one axis and the coincident γ rays from the four detectors at forward and backward θ angles (F/B) on the other. The quantity

$$R_{DCO} = \frac{I_\gamma(F/B, \sim 90^\circ)}{I_\gamma(\sim 90^\circ, F/B)} \quad (1)$$

was measured for various transitions in ^{108}In and ^{110}In , where $I_\gamma(i,j)$ is the intensity of a transition on the i axis of the DCO matrix measured after gating on a transition on the j axis. To determine the multipolarities of given transitions, these R_{DCO} values were compared with expected ratios, shown in Table II, calculated [20] for the configuration of the detectors in the Stony Brook array. The predictions made for

TABLE II. Calculated R_{DCO} values for the Stony Brook array, assuming a Gaussian distribution of spin substates with $\sigma_I/I=0.3$. The quoted limits for the mixed $M1/E2$ transitions correspond to the minimum and maximum R_{DCO} values obtained through $E2$ admixture.

Observed transition multipolarity	R_{DCO} , $\Delta I=1$ pure dipole gate	R_{DCO} , $\Delta I=2$ quadrupole gate
$\Delta I=2$ quadrupole	2.0	1.0
$\Delta I=1$ pure dipole	1.0	0.5
$\Delta I=0$ pure dipole	2.0	1.0
$\Delta I=1$ mixed $M1/E2$	$0.4 < R < 2.5$	$0.2 < R < 1.4$
$\Delta I=0$ mixed $M1/E2$	$1.0 < R < 2.3$	$0.5 < R < 1.2$

the DCO ratios were tested by calculating R_{DCO} values for known transitions in neighboring nuclei populated in these reactions and were found to be consistent with the expected values.

(iii) Additional angle-dependent matrices were sorted from both backed-target data sets in order to perform DSAM lifetime analyses. For the ^{108}In experiment, two matrices were sorted: one with γ rays from the detector at 26° on one axis (the “ θ axis”) versus all detectors on the other axis (the “all axis”) and another with γ rays from the detector at 142° versus all detectors. Only one each of the forward and backward detectors was used for the ^{108}In DSAM analysis to take advantage of superior intrinsic resolution in these detectors; even with a single detector, however, there were enough counts in the spectra to perform a line-shape analysis. For the ^{110}In data, matrices were sorted for all forward- and backward-angle detectors. Separate matrices with $\sim 90^\circ$ versus all were not created in either analysis; instead, the DCO matrices described above were used, with the F/B axes acting as the “all axes” of $\sim 90^\circ$ -versus-all DSAM matrices. Background-subtracted spectra were generated for each angle by gating on the “all axis” of each matrix at energies corresponding to transitions in ^{108}In or ^{110}In with fully stopped peaks. Those transitions that exhibited Doppler-broadened line shapes could be fitted using the LINESHAPE code of Wells and Johnson [21], from which lifetimes, and ultimately $B(M1)$ or $B(E2)$ transition strengths, could be extracted. This is discussed further in Sec. IV C.

IV. RESULTS

The level schemes for ^{108}In and ^{110}In deduced from both the thin- and backed-target E_γ - E_γ matrices are presented in Figs. 2 and 3, respectively. Although the relative population of high-spin states in the thin- and backed-target experiments differed, the results have been combined into a single level scheme for each nucleus. The extracted properties of the transitions are listed in Tables III and IV for ^{108}In and ^{110}In , respectively. In both level schemes, the sequences of γ rays have been labeled and are referred to as bands to facilitate discussion and to make comparisons between the two isotopes; these labels do not necessarily imply a collective nature for the states in question.

A. ^{108}In level scheme

High-spin states in the nucleus ^{108}In had been studied previously by Elias *et al.* [22], Andersson *et al.* [23], and Chakrawarthy *et al.* [24]. The majority of the ^{108}In level scheme deduced in the previous works has been confirmed. Those portions of the level scheme which have been extended or modified in the current studies are discussed in detail below.

1. Bands 1 and 6

The sequence of γ rays labeled band 1 in Fig. 2 consists of a negative-parity band with an $I^\pi=8^-$ bandhead feeding into the $I^\pi=7^+$ ground state via a 1119-keV transition. The transitions identified in Refs. [22–24] for this band have been confirmed, including the crossover transitions. Additionally, 636- and 438-keV transitions have been observed to feed in parallel into the top of this band.

The multipolarity of the 1119-keV transition was previously shown to be $E1$, as discussed in Ref. [22] and references therein; this pure dipole transition was, therefore, a useful gating transition on the DCO matrix for determining multipolarities of other, select γ rays, as indicated in Table III. The DCO ratios for the 213-, 529-, 604-, 541-, and newly added 636-keV transitions suggest each has mixed $M1/E2$ multipolarity. The corresponding spin assignments confirm those of Ref. [24]. The measured R_{DCO} also indicates that the 213-keV γ ray has a mixing ratio $\delta \approx 0$, in agreement with the conversion-electron measurement of Elias *et al.* (see also Table 1 of Ref. [22]). The approximate purity of the 213-keV transition and larger detector efficiency at the low γ -ray energy (compared to the 1119-keV γ ray) makes this transition a more suitable gate for further DCO analysis. This transition is also a clean gate, as evidenced by the spectrum in Fig. 4. Where possible, results from both a 213-keV and a 1119-keV gate were compared for consistency.

The observation of band 6 in this study confirms the coincidence relationships suggested by the sequence of γ rays with energies 150, 656, 749, and 958 keV feeding out of band 3 in Ref. [24], although the ordering of the transitions presented in that analysis has not been confirmed. In this work, the 150-keV γ ray has been placed directly above the 7^+ ground state on the basis of the mutual coincidence of the 150-keV γ ray with all of the members of band 1, but not with the 1119-keV γ ray. Figure 5(a) shows a low-energy portion of the spectrum gated on 1119 keV; no peak is present at 150 keV. On the other hand, in Fig. 5(b), which shows a spectrum gated on 969 keV, the 150-keV peak is present. This demonstrates that if the 150-keV peak was present in the 1119-keV gate, the peak could have been resolved from the 147- and 154-keV peaks of band 2. The 969-keV transition was also found to be in coincidence with all of the members of band 1, but not the 1119-keV γ ray, confirming that the 150- and 969-keV transitions decay parallel to the 1119-keV transition. The placement of the 656-keV transition has been corrected based on the observation of a 312-keV transition in coincidence with band 1 and the 656-keV transition. The remaining two γ rays in the sequence, with energies 749 and 958 keV, have been ordered

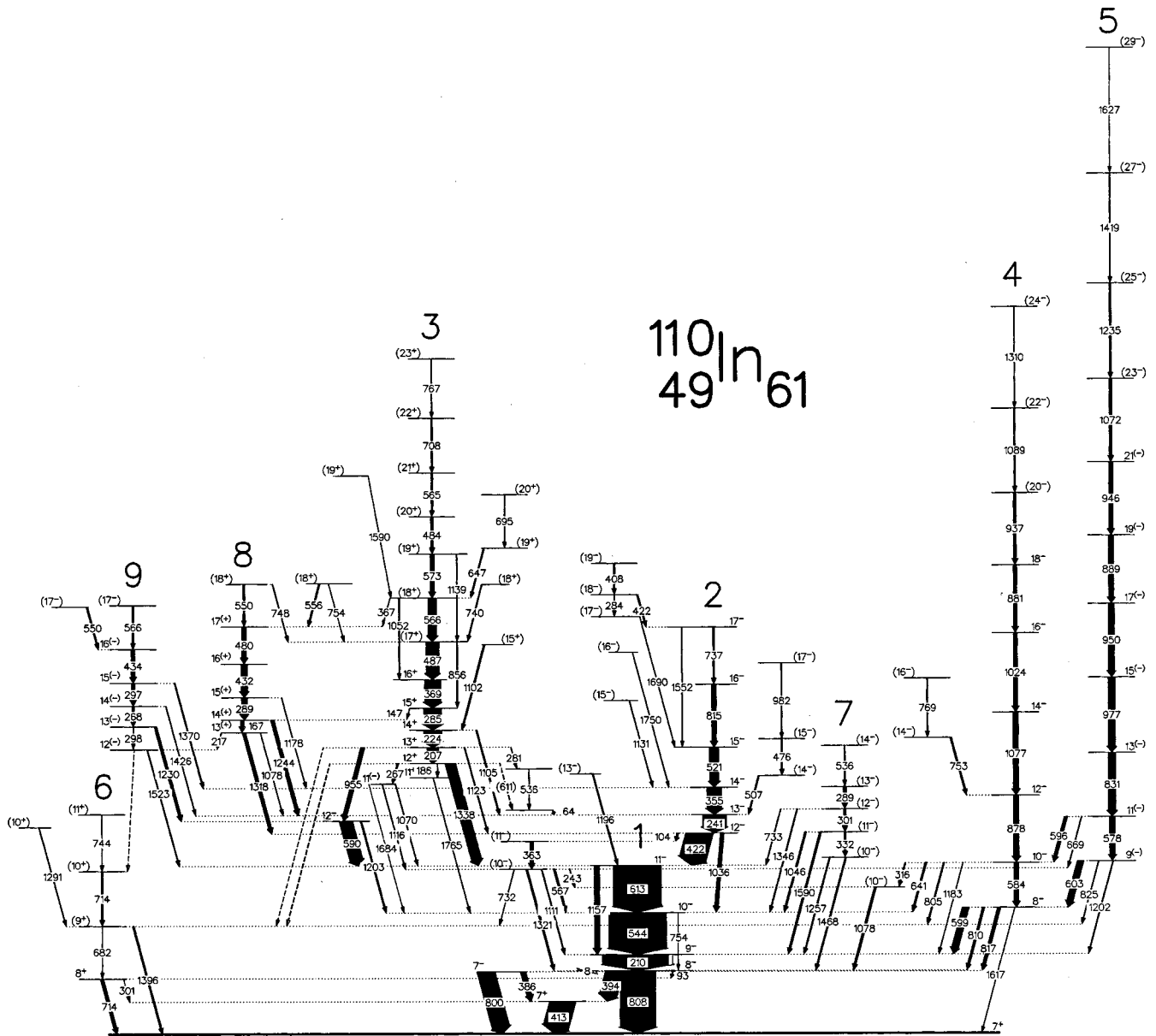


FIG. 3. Level scheme of ^{110}In deduced from the backed- and thin-target data. The width of each arrow is proportional to the intensity of the transition. Intensity associated with internal conversion (unobserved) is represented by the white portion of the arrow.

3. Band 3

Band 3 was shown in Ref. [24] to be a sequence of mixed $M1/E2$ transitions extending up to spin $19\hbar$. The current study extends this band up to $22\hbar$ by two parallel sequences feeding into the $I=19$ state, with most of the intensity flowing through the 524-596-740-keV sequence; this branch has, therefore, been placed as the continuation of the band. Two weak crossover transitions were observed in this band, confirming the ordering of the γ rays up to the $I=19$ state. This work confirms the existence of four transitions linking this band to band 2. The values of R_{DCO} extracted for these linking γ rays in the current study indicate that they are $I \rightarrow I-1$ transitions with $\delta \approx 0$. No distinction could be made between $E1$ and nearly pure $M1$ multiplicities on the basis of these measurements alone; therefore, the results of the

polarization measurements made in Ref. [24] have been adopted, assigning $E1$ multiplicity to these transitions and giving band 3 positive parity.

4. Bands 4 and 5

A 1861-keV transition has been observed which is not in coincidence with transitions in any of the bands discussed thus far. Figure 6 shows a spectrum gated on this transition. All of the transitions labeled in this spectrum are also coincident with band-1 transitions, conclusively associating the 1861-keV and coincident transitions with ^{108}In . The 1861-keV γ ray has been placed directly feeding the 7^+ ground state. Most of the γ rays labeled in Fig. 6 were found to be in mutual coincidence. These γ rays have been organized into two bands, labeled 4 and 5 in Fig. 2, based on coincidence,

TABLE III. Properties of transitions observed in the ^{108}In thin- and backed-target experiments. Intensities are corrected for detector efficiency and normalized to 100% for the 213-keV transition. The R_{DCO} values are from the backed-target data only. Unless otherwise noted, the values in column 4 are from gates on the pure dipole (D) 1119- and/or 213-keV transitions, and the values in column 5 are from gates on the pure quadrupole (Q) transitions in band 5.

E_γ (keV)	$I_{\gamma,thin}$	$I_{\gamma,backed}$	$R_{DCO}(D)$	$R_{DCO}(Q)$	$I_i^\pi \rightarrow I_f^\pi$	$M\lambda$	Band
147.0(1)	37.6(11)	53.9(16)	0.97(2)		$11^- \rightarrow 10^-$	$M1/E2$	2
150.4(1)	8.3(8)	29.0(6)	1.68(6)	0.98(6) ^a	$7^+ \rightarrow 7^+$	$M1/E2$	6 \rightarrow 1
153.5(1)	60.2(18)	87.5(27)	0.96(1)		$12^- \rightarrow 11^-$	$M1/E2$	2
186.2(1)	2.5(1)	2.5(1)	1.09(17)		$14^+ \rightarrow 13^+$	$M1/E2$	3
213.1(1)	100.0(31)	100.0(31)	0.94(1)	0.50(5)	$9^- \rightarrow 8^-$	$M1/E2$	1
223.3(1)	7.3(3)	7.0(3)	0.85(10)		$12^- \rightarrow 11^-$	$M1/E2$	7
230.8(1)	85.6(26)	95.5(29)	0.97(1)		$13^- \rightarrow 12^-$	$M1/E2$	2
237.0(1)		29.2(9)			$11^+ \rightarrow 9^+$	$E2$	8
255.9(1)	12.9(4)	10.8(3)	0.92(4)		$15^+ \rightarrow 14^+$	$M1/E2$	3
290.3(1)	2.1(8)	1.5(1)			$10^- \rightarrow$		
293.7(1)	6.2(2)	5.1(2)	0.88(5) ^b		$11^- \rightarrow 10^-$	$M1/E2$	2 \rightarrow 7
307.1(1)		0.7(1)			$\rightarrow 15$		$\rightarrow 5$
311.6(1)	1.0(1)	1.8(1)	1.57(31)		$8^- \rightarrow 8^+$	$E1$	1 \rightarrow 6
322.2(1)	13.0(5)	10.8(4)	0.77(14)	0.41(3) ^a	$13^- \rightarrow 12^-$	$M1/E2$	7
335.4(1)	60.5(18)	62.6(19)	0.99(2)		$14^- \rightarrow 13^-$	$M1/E2$	2
341.9(3)	2.4(2)	0.4(1)			$12^- \rightarrow$		7 \rightarrow
349.1(1)	15.6(5)	14.7(5)	1.03(3)		$12^- \rightarrow 11^-$	$M1/E2$	2 \rightarrow 1
357.3(1)	21.2(7)	16.8(5)	0.92(4)		$16^+ \rightarrow 15^+$	$M1/E2$	3
361.6(1)	0.7(1)	1.6(1)			$10^{(-)} \rightarrow 9^{(-)}$	$M1/E2$	4 \rightarrow
410.6(1)	1.6(1)	1.5(1)	0.92(12)		$15^{(-)} \rightarrow 14^{(-)}$	$M1/E2$	
413.7(1)	10.5(4)	8.5(3)	0.99(11)	0.51(5) ^a	$14^- \rightarrow 13^-$	$M1/E2$	7
415.5(1)	2.3(1)	1.6(1)			$(17^-) \rightarrow (16^-)$	$M1/E2$	
437.9(1)	2.4(2)	2.1(2)			$(13^-) \rightarrow 12^-$	$M1/E2$	$\rightarrow 1$
443.8(1)	3.3(3)	2.7(1)		0.47(6) ^a	$13^{(+)} \rightarrow 12^+$	$M1/E2$	8
462.0(1)	1.4(1)	1.4(1)			$(18^-) \rightarrow (17^-)$	$M1/E2$	
473.0(1)	22.3(7)	14.2(4)	0.87(4)		$17^+ \rightarrow 16^+$	$M1/E2$	3
493.3(1)	1.7(1)	1.0(1)			$(19^-) \rightarrow (18^-)$	$M1/E2$	
506.0(1)	3.4(2)	2.6(2)	1.24(21)		$10^- \rightarrow 10^-$	$M1/E2$	$\rightarrow 1$
511.0(1)	6.0(4)	10.8(5)	1.38(10)		$11^- \rightarrow 10^-$	$M1/E2$	7 \rightarrow
524.0(1)	11.7(4)	5.3(2)			$(20^+) \rightarrow 19^+$	$M1/E2$	3
527.7(1)		3.8(2)	1.07(1) ^c		$8^{(-)} \rightarrow 9^-$	$M1/E2$	4 \rightarrow 1
527.8(1)	35.1(11)	31.6(10)	1.07(1) ^c		$15^- \rightarrow 14^-$	$M1/E2$	2
528.6(1)	54.0(17)	45.4(15)	1.07(1) ^c		$10^- \rightarrow 9^-$	$M1/E2$	1
541.5(1)	16.7(6)	14.2(5)	0.90(4) ^d		$12^- \rightarrow 11^-$	$M1/E2$	1
542.4(1)	9.7(3)	4.3(2)			$19^+ \rightarrow 18^+$	$M1/E2$	3
542.5(3)	1.1(2)	0.3(1)			$(22^+) \rightarrow (21^+)$	$M1/E2$	
553.1(1)	4.3(2)	4.1(2)		0.89(13)	$13 \rightarrow 11$	$E2$	5
564.4(1)	17.3(5)	8.1(3)	0.58(7)		$18^+ \rightarrow 17^+$	$M1/E2$	3
570.7(1)		2.9(2)			$\rightarrow 10^{(-)}$		$\rightarrow 4$
575.5(1)	3.0(2)	1.1(1)			$(16^-) \rightarrow 15^-$	$M1/E2$	$\rightarrow 2$
576.0(1)	2.9(1)	0.7(1)			$(20^+) \rightarrow 19^+$	$M1/E2$	$\rightarrow 3$
577.3(2)	5.3(2)	1.3(1)		0.94(5) ^e	$10^{(-)} \rightarrow 10^-$	$M1/E2$	4 \rightarrow 1
577.9(1)	8.3(4)	13.3(5)		0.94(5) ^e	$10^{(-)} \rightarrow 8^{(-)}$	$E2$	4
585.1(1)	14.4(5)	7.2(3)	0.70(9)		$17^- \rightarrow 16^-$	$M1/E2$	2
588.7(1)		2.7(2)			$9^+ \rightarrow 8^+$	$M1/E2$	8 \rightarrow 6
596.0(1)	7.6(3)	2.8(1)			$(21^+) \rightarrow (20^+)$	$M1/E2$	3
604.3(1)	34.9(11)	31.2(10)	1.13(3)		$11^- \rightarrow 10^-$	$M1/E2$	1
613.4(1)	3.3(2)	2.8(1)			$15 \rightarrow 14^{(-)}$	$M1/E2$	5 \rightarrow 4
625.9(1)	3.3(3)	3.1(2)			$11^- \rightarrow$		7 \rightarrow

TABLE III. (*Continued.*)

E_γ (keV)	$I_{\gamma,thin}$	$I_{\gamma,backed}$	$R_{DCO}(D)$	$R_{DCO}(Q)$	$I_i^\pi \rightarrow I_f^\pi$	$M\lambda$	Band
632.5(1)	2.1(3)	3.1(2)			$(15^-) \rightarrow 14^-$	$M1/E2$	7
635.5(1)	3.9(2)	2.7(2)	1.26(16)		$13^- \rightarrow 12^-$	$M1/E2$	1
656.5(1)	11.0(4)	21.6(7)	1.55(13) ^b		$8^+ \rightarrow 7^+$	$M1/E2$	6
660.9(1)	18.8(6)	12.7(4)	0.94(7)		$16^- \rightarrow 15^-$	$M1/E2$	2
728.6(2)	1.6(1)	0.3(1)			$(21^+) \rightarrow (20^+)$	$M1/E2$	
735.9(1)	3.8(2)	2.1(1)			$(18^-) \rightarrow 17^-$	$M1/E2$	$\rightarrow 2$
740.3(3)	2.2(1)	0.5(1)			$(22^+) \rightarrow (21^+)$	$M1/E2$	3
741.6(1)	0.1(2)	3.3(2)			$8^{(-)} \rightarrow 8^-$	$M1/E2$	$4 \rightarrow 1$
749.2(1)	6.1(3)	9.1(3)	1.30(13) ^b		$9^+ \rightarrow 8^+$	$M1/E2$	6
753.4(1)	0.8(2)	1.4(2)			$(7^-) \rightarrow 7^+$	$E1$	$\rightarrow 6$
777.8(1)	17.6(6)	15.5(5)	2.08(20)	1.02(8)	$15 \rightarrow 13$	$E2$	5
782.0(1)	3.1(2)	3.0(2)	2.08(27)		$15^- \rightarrow 13^-$	$E2$	$\rightarrow 2$
800.3(1)	3.5(2)	3.1(1)	1.55(25) ^b		$11^- \rightarrow 10^-$	$M1/E2$	$2 \rightarrow 1$
804.1(1)	6.6(3)	4.6(2)		0.94(13)	$19 \rightarrow 17$	$E2$	$5 \rightarrow$
804.8(2)	1.2(3)	0.9(1)			$13^- \rightarrow 12^+$	$E1$	$7 \rightarrow 8$
827.0(1)	11.9(5)	10.0(4)	1.44(15) ^f	0.52(9) ^g	$13 \rightarrow 12^{(-)}$	$M1/E2$	$5 \rightarrow 4$
828.3(1)	11.5(4)	7.9(2)	1.44(15) ^f		$17 \rightarrow 15$	$E2$	5
834.7(1)	18.4(7)	19.0(7)	1.76(18)	1.10(10)	$12^{(-)} \rightarrow 10^{(-)}$	$E2$	4
864.2(1)		2.0(1)			$15^- \rightarrow 13^-$	$E2$	2
904.2(1)	10.2(4)	7.2(3)		1.05(10)	$19 \rightarrow 17$	$E2$	5
905.3(2)		0.5(1)			$(7^-) \rightarrow 7^+$	$E1$	$\rightarrow 1$
926.0(1)	4.3(2)	3.3(2)	1.54(27)		$14^{(-)} \rightarrow 13^-$	$M1/E2$	$\rightarrow 2$
928.2(1)	7.3(3)	6.0(2)	1.58(39)	1.02(10)	$17 \rightarrow 15$	$E2$	$\rightarrow 5$
956.7(1)	0.1(2)	3.5(2)			$8^{(-)} \rightarrow (7^-)$	$M1/E2$	$4 \rightarrow$
957.8(1)	7.2(2)	8.6(3)	1.10(11) ^b		$10^- \rightarrow 9^+$	$E1$	$2 \rightarrow 6$
958.0(3)	1.2(7)	0.5(2)			$9^{(-)} \rightarrow 8^-$	$M1/E2$	$\rightarrow 1$
968.7(1)	5.2(8)	7.4(1)	0.91(9)		$8^- \rightarrow 7^+$	$E1$	$1 \rightarrow 6$
971.7(1)	2.0(2)	1.8(1)			$10^- \rightarrow 9^+$	$E1$	$\rightarrow 8$
984.5(1)	4.8(2)	1.6(1)	1.48(29)		$18^+ \rightarrow 17^+$	$M1/E2$	$\rightarrow 3$
987.0(1)	5.0(6)	4.3(2)		0.63(6) ^a	$12^+ \rightarrow 11^+$	$M1/E2$	8
991.5(1)	6.1(4)	4.5(2)		0.95(26)	$14^{(-)} \rightarrow 12^{(-)}$	$E2$	4
1002.4(1)	9.7(4)	4.6(2)		0.95(13)	$21 \rightarrow 19$	$E2$	5
1017.9(2)	1.2(1)	1.1(1)	1.34(42)		$11^- \rightarrow 10^-$	$M1/E2$	$7 \rightarrow 1$
1028.2(1)	2.1(2)	2.2(1)	2.15(47) ^b	0.79(21) ^a	$11^- \rightarrow 11^+$	$E1$	$2 \rightarrow 8$
1035.1(1)	4.8(3)	2.5(2)			$10^- \rightarrow 9^-$	$M1/E2$	$\rightarrow 1$
1038.8(1)	2.3(2)	1.3(1)			$18^+ \rightarrow 16^+$	$E2$	3
1043.0(1)	4.6(3)	4.6(2)		0.48(12)	$10^{(-)} \rightarrow 9^+$	$E1$	$4 \rightarrow 8$
1098.4(6)	3.6(4)	0.5(2)			$\rightarrow 9^-$		$\rightarrow 1$
1106.6(1)	4.1(2)	3.6(2)			$10^{(-)} \rightarrow 9^-$	$M1/E2$	$4 \rightarrow 1$
1107.7(1)	1.1(1)	1.0(1)			$19^+ \rightarrow 17^+$	$E2$	3
1108.7(1)	4.5(5)	4.5(3)			$11 \rightarrow 10^{(-)}$	$M1/E2$	$5 \rightarrow 4$
1119.4(1)	74.4(34)	156.6(10)	1.06(2)		$8^- \rightarrow 7^+$	$E1$	1
1133.8(1)	4.6(3)	4.8(3)	1.77(16)		$11^- \rightarrow 9^-$	$E2$	1
1146.7(2)	0.4(3)	1.4(2)			$12^- \rightarrow 10^-$	$E2$	1
1159.9(4)	1.0(1)				$\rightarrow 18^+$		
1179.0(1)	6.1(3)	2.0(1)			$(23) \rightarrow 21$	$E2$	5
1182.2(1)	18.7(6)	18.9(6)	2.50(10)		$10^- \rightarrow 9^-$	$M1/E2$	$2 \rightarrow 1$
1189.1(1)		1.4(1)			$16^- \rightarrow 14^-$	$E2$	2
1220.5(1)	3.1(1)	2.5(1)	1.38(46)		$16^+ \rightarrow 15^-$	$E1$	$3 \rightarrow 2$
1245.9(1)		3.6(2)		1.04(15) ^a	$9^+ \rightarrow 7^+$	$E2$	$8 \rightarrow 6$
1246.9(1)		1.0(1)			$17^- \rightarrow 15^-$	$E2$	2
1248.8(2)	1.2(2)	1.2(1)			$10^- \rightarrow 8^-$	$E2$	$\rightarrow 1$
1256.1(5)		0.7(2)			$\rightarrow 11^-$		$\rightarrow 7$

TABLE III. (Continued.)

E_γ (keV)	$I_{\gamma,thin}$	$I_{\gamma,backed}$	$R_{DCO}(D)$	$R_{DCO}(Q)$	$I_i^\pi \rightarrow I_f^\pi$	$M\lambda$	Band
1284.3(1)	0.5(3)	1.6(2)			$\rightarrow 9^-$		$\rightarrow 1$
1329.5(1)	18.7(6)	21.8(7)	1.97(13)		$11^- \rightarrow 9^-$	$E2$	$2 \rightarrow 1$
1343.7(1)	1.0(2)	1.1(1)			$(15^+) \rightarrow 13^{(+)}$	$E2$	8
1391.0(1)	10.2(3)	8.1(3)	0.90(10)		$15^+ \rightarrow 14^-$	$E1$	$3 \rightarrow 2$
1396.0(1)	22.7(7)	24.5(8)	1.89(11)		$10^- \rightarrow 8^-$	$E2$	$2 \rightarrow 1$
1396.8(1)	7.2(8)	33.4(19)		1.11(4) ^a	$9^+ \rightarrow 7^+$	$E2$	$8 \rightarrow 1$
1406.5(1)		2.8(1)			$9^+ \rightarrow 7^+$	$E2$	6
1469.4(1)	4.6(3)	4.1(2)		0.60(7) ^a	$12^- \rightarrow 11^+$	$E1$	$7 \rightarrow 8$
1470.5(1)	9.8(3)	9.9(3)	1.04(9)		$14^+ \rightarrow 13^-$	$E1$	$3 \rightarrow 2$
1515.3(1)	2.3(2)	1.9(1)	0.89(22)		$13^+ \rightarrow 12^-$	$E1$	$3 \rightarrow 2$
1581.4(10)		0.2(1)			$(17^-) \rightarrow 15^-$	$E2$	$\rightarrow 2$
1608.9(1)		1.1(1)			$(19^+) \rightarrow 17^+$	$E2$	$\rightarrow 3$
1694.8(1)	1.8(1)	2.7(1)			$(16^-) \rightarrow 14^-$	$E2$	$\rightarrow 2$
1709.5(1)	0.4(1)	1.3(1)			$\rightarrow 15^-$		
1774.8(2)		0.5(1)			$\rightarrow 15^-$		
1861.5(1)	0.3(6)	7.3(4)		0.52(4)	$8^- \rightarrow 7^+$	$E1$	$4 \rightarrow 1$

^a R_{DCO} from gate on 237-keV transition.

^b R_{DCO} from gate on 231-keV nearly pure dipole transition.

^cFit to composite ~ 528 -keV peak, including the tentative 527.7-keV transition. See text for details.

^dIncludes small contributions from the 542.4- and 542.5-keV transitions.

^eFit to composite ~ 578 -keV peak, including the tentative 577.3-keV transition. See text for details.

^fFit to composite ~ 828 -keV peak. See text for details.

^g R_{DCO} from summed gate on 804- and 928-keV transitions of side branch associated with band 5.

energy-sum, and intensity-balance arguments. Band 5 decays exclusively to band 4, which subsequently decays to the ground state through the 1861-keV transition, as well as through multiple decay paths to band 1. Note that the peak at ~ 828 keV is a doublet. Spectra gated on the 553-, 1109-, 613-, 992-, 804-, and 928-keV γ rays associated with bands 4 and 5 indicated smaller relative intensities for the ~ 828 -keV peak than was observed in spectra gated on the other γ rays associated with these bands. This strongly suggests that each γ ray in the aforementioned list of gating transitions is in coincidence with only one member of the doublet. The placement of the transitions of this doublet was primarily determined based on these observed intensities. The current placement of the transitions in these bands is a considerable modification of band 5 from Ref. [24], particularly the reorganization into two separate bands. In addition, the 828-904-keV and 928-804-keV sequences of γ rays, placed in mutual coincidence in [24], have been placed as parallel decay paths in band 5. The former sequence is more intense and has been placed as the in-band branch.

Coincidences between bands 1 and 4 indicate that band 4 feeds into band 1 at the $I^\pi = 9^-$ state or higher. The 1861-keV state in band 4 is nearly degenerate with the 10^- state of band 1, which makes discerning the specific decay paths very difficult; band 4 could feed into band 1 via a 577-keV γ ray parallel to the in-band 578-keV γ ray, via a 528-keV γ ray feeding into the 9^- state of band 1, or possibly both. The level scheme in Fig. 2 has been drawn with both of these transitions tentatively placed.

The DCO ratios for the 835-keV (band 4) and 778-keV (band 5) transitions indicate $E2$ multipolarity for these γ rays (see Table III). R_{DCO} values were measured with gates on the 778- and 835-keV transitions to enhance the measurements for the remaining transitions in bands 4 and 5 and to determine the multipolarity of the transitions feeding parallel to the 213- and 1119-keV γ -ray gates. These results are also summarized in Table III.

The 1861-keV transition is consistent with a stretched (pure) dipole multipolarity. In Ref. [24], Chakravarthy *et al.* assigned this γ ray $E3$ multipolarity, with the 1861-keV level having $I^\pi = 10^-$. With this assignment, the 10^- levels of bands 1 and 4 are within 1 keV of each other. Such close proximity of two levels with the same quantum numbers typically results in large admixtures of the two states. Such large admixtures are usually observed experimentally as significant crosstalk involving the two nearly degenerate levels. Band 4 decays to band 1, but band 1 has not been observed to decay to band 4. Chakravarthy *et al.* also point out the absence of a Doppler-broadened line shape for the 1861-keV transition as support for their $E3$ assignment [24]. In the current analysis, the lowest transition in bands 4 and 5 that was found to have a measurable line shape was the 1002-keV transition, suggesting that the long lifetime, implied by the absence of line shapes, in fact exists significantly higher in the sequence (although this does not necessarily rule out a long lifetime for the 1861-keV state as well). This will be discussed further in Secs. IV C and V B. In this work, $E1$ multipolarity has been assigned to the 1861-keV transition and, hence, $I^\pi = 8^{(-)}$ to the 1861-keV state of band 4.

TABLE IV. Properties of transitions observed in the ^{110}In thin- and backed-target experiments. Intensities are corrected for detector efficiency and normalized to 100% for the 210-keV transition. The R_{DCO} values are from the backed-target data only. Unless otherwise noted, the values in column 4 are from gates on the pure dipole (D) 544- and/or 210-keV transitions, and the values in column 5 are from gates on the pure quadrupole (Q) 878- or 977-keV transitions.

E_γ (keV)	$I_{\gamma,thin}$	$I_{\gamma,backed}$	$R_{DCO}(D)$	$R_{DCO}(Q)$	$I_i^\pi \rightarrow I_f^\pi$	$M\lambda$	Band
8.0(10) ^a	0.2(1)	0.3(1)			$8^- \rightarrow 7^-$	$M1/E2$	1
63.9(1)	0.5(1)	4.7(3)			$\rightarrow 13^-$		$\rightarrow 2$
93.2(1)	0.9(1)	1.6(1)			$8^- \rightarrow 8^+$	$E1$	$1 \rightarrow 6$
104.2(1)	1.9(1)	2.2(1)			$12^- \rightarrow (11^-)$	$M1/E2$	$2 \rightarrow$
147.4(1)	0.5(1)	0.4(1)			$15^+ \rightarrow 14^{(+)}$	$M1/E2$	$3 \rightarrow 8$
166.9(1)	4.3(1)	3.3(1)	0.68(8)		$14^{(+)} \rightarrow 13^{(+)}$	$M1/E2$	8
185.6(1)	1.0(1)	0.7(1)	1.29(24) ^b		$12^+ \rightarrow 11^+$	$M1/E2$	3
207.5(1)	16.9(5)	14.6(5)	1.02(5)		$13^+ \rightarrow 12^+$	$M1/E2$	3
209.5(1)	100.0(30)	100.0(30)	1.04(2)	0.63(13)	$9^- \rightarrow 8^-$	$M1/E2$	1
217.2(1)	1.1(1)	0.6(1)	0.97(11) ^c		$13^{(+)} \rightarrow 12^{(-)}$	$E1$	$8 \rightarrow 9$
223.8(1)	26.6(8)	19.8(6)	0.90(3)		$14^+ \rightarrow 13^+$	$M1/E2$	3
241.1(1)	34.6(10)	30.4(9)	0.89(2)		$13^- \rightarrow 12^-$	$M1/E2$	2
243.0(1)	1.0(1)	1.0(1)			$(10^-) \rightarrow (10^-)$	$M1/E2$	
267.2(1)	2.1(1)	1.3(1)	0.85(9) ^d		$12^+ \rightarrow 11^{(-)}$	$E1$	$3 \rightarrow$
268.0(1)	3.9(1)	2.8(1)	0.68(11)		$14^{(-)} \rightarrow 13^{(-)}$	$M1/E2$	9
281.3(1)	0.6(1)	0.9(1)			$13^+ \rightarrow$		$3 \rightarrow$
284.0(1)	1.2(1)	0.8(1)			$(18^-) \rightarrow (17^-)$	$M1/E2$	
285.4(1)	26.5(8)	18.5(6)	0.85(3)		$15^+ \rightarrow 14^+$	$M1/E2$	3
288.5(1)	4.3(2)	4.0(2)	0.92(5) ^e		$(13^-) \rightarrow (12^-)$	$M1/E2$	7
289.0(1)	9.3(3)	6.5(2)	0.92(5) ^e		$15^{(+)} \rightarrow 14^{(+)}$	$M1/E2$	8
297.3(1)	4.8(2)	2.8(1)	0.63(10) ^f		$15^{(-)} \rightarrow 14^{(-)}$	$M1/E2$	9
297.8(1)	1.1(1)	0.8(1)	0.63(10) ^f		$13^{(-)} \rightarrow 12^{(-)}$	$M1/E2$	9
300.9(1)	0.6(1)	0.6(1)			$8^+ \rightarrow 7^+$	$M1/E2$	$6 \rightarrow 1$
301.3(1)	3.6(1)	2.6(1)	0.89(19) ^g		$(12^-) \rightarrow (11^-)$	$M1/E2$	7
315.6(1)	1.7(1)	1.4(1)		0.98(19)	$10^- \rightarrow (10^-)$	$M1/E2$	$4 \rightarrow$
331.5(1)	2.9(1)	1.7(1)	0.88(16) ^h		$(11^-) \rightarrow (10^-)$	$M1/E2$	7
354.6(1)	22.2(7)	16.6(5)	0.77(4)		$14^- \rightarrow 13^-$	$M1/E2$	2
363.3(1)	5.3(2)	3.7(2)	0.96(25) ^g		$(11^-) \rightarrow (10^-)$	$M1/E2$	
366.9(1)	0.8(1)	0.7(1)			$(18^+) \rightarrow 17^{(+)}$	$M1/E2$	$3 \rightarrow 8$
369.0(1)	24.4(7)	13.6(4)	0.69(5)		$16^+ \rightarrow 15^+$	$M1/E2$	3
386.2(1)	8.0(3)	8.6(3)	2.14(16)		$7^- \rightarrow 7^+$	$E1$	1
394.5(1)	27.1(9)	26.1(8)	0.94(4)		$8^- \rightarrow 7^+$	$E1$	1
408.2(1)	2.1(1)	0.7(1)			$(19^-) \rightarrow (18^-)$	$M1/E2$	
413.4(1)	38.6(4)	35.9(5)	1.75(6)		$7^+ \rightarrow 7^+$	$M1/E2$	1
421.9(1)	40.6(12)	33.8(10)	0.87(2)		$12^- \rightarrow 11^-$	$M1/E2$	$2 \rightarrow 1$
422.0(1)	2.3(1)	1.1(1)			$(18^-) \rightarrow 17^-$	$M1/E2$	$\rightarrow 2$
432.4(1)	9.7(3)	5.7(2)	0.75(21)		$16^{(+)} \rightarrow 15^{(+)}$	$M1/E2$	8
433.8(1)	5.7(2)	2.7(1)	0.53(11) ⁱ		$16^{(-)} \rightarrow 15^{(-)}$	$M1/E2$	9
476.4(1)	2.1(1)				$(15^-) \rightarrow (14^-)$	$M1/E2$	
480.5(1)	7.0(2)	3.2(1)			$17^{(+)} \rightarrow 16^{(+)}$	$M1/E2$	8
483.9(1)	3.9(1)	2.7(1)			$(20^+) \rightarrow (19^+)$	$M1/E2$	3
486.9(1)	19.7(6)	8.4(3)			$(17^+) \rightarrow 16^+$	$M1/E2$	3
506.8(1)	1.9(1)				$(14^-) \rightarrow 13^-$	$M1/E2$	$\rightarrow 2$
521.1(1)	13.6(4)	7.6(2)	0.62(7)		$15^- \rightarrow 14^-$	$M1/E2$	2
536.0(2)	0.9(1)	0.3(1)					
536.0(1)	1.6(1)	0.6(1)			$(14^-) \rightarrow (13^-)$	$M1/E2$	7
543.7(1)	87.2(26)	73.0(22)	1.04(4) ^g		$10^- \rightarrow 9^-$	$M1/E2$	1
550.2(1)	2.6(1)	0.9(1)			$(18^+) \rightarrow 17^{(+)}$	$M1/E2$	8
550.3(1)	2.2(1)	0.9(1)			$(17^-) \rightarrow 16^{(-)}$	$M1/E2$	$\rightarrow 9$
555.9(1)	2.1(1)	0.4(1)			$(18^+) \rightarrow 17^{(+)}$	$M1/E2$	$\rightarrow 8$
565.4(1)	2.8(2)	0.6(1)			$(21^+) \rightarrow (20^+)$	$M1/E2$	3

TABLE IV. (Continued.)

E_γ (keV)	$I_{\gamma,thin}$	$I_{\gamma,backed}$	$R_{DCO}(D)$	$R_{DCO}(Q)$	$I_i^\pi \rightarrow I_f^\pi$	$M\lambda$	Band
565.6(1)	13.0(4)	4.0(1)			$(18^+) \rightarrow (17^+)$	$M1/E2$	3
566.1(1)	2.3(1)	0.7(1)			$(17^-) \rightarrow 16^{(-)}$	$M1/E2$	9
567.2(1)	3.1(2)	3.6(2)			$(10^-) \rightarrow 10^-$	$M1/E2$	$\rightarrow 1$
572.9(1)	6.2(2)	2.1(1)			$(19^+) \rightarrow (18^+)$	$M1/E2$	3
578.0(1)	8.3(3)	7.0(3)		1.08(14)	$11^{(-)} \rightarrow 9^{(-)}$	$E2$	5
584.4(1)	7.4(3)	6.1(2)		0.89(10)	$10^- \rightarrow 8^-$	$E2$	4
590.1(1)	20.0(6)	11.8(4)	0.99(8)		$12^- \rightarrow 11^-$	$M1/E2$	$\rightarrow 1$
596.2(1)	5.1(2)	3.9(2)		0.43(8)	$11^{(-)} \rightarrow 10^-$	$M1/E2$	$5 \rightarrow 4$
599.3(1)	10.2(4)	7.7(3)	1.22(24) ^g	0.77(15)	$8^- \rightarrow 9^-$	$M1/E2$	$4 \rightarrow 1$
603.2(1)	9.8(4)	7.6(3)	0.84(19) ^g	0.42(6)	$9^{(-)} \rightarrow 8^-$	$M1/E2$	$5 \rightarrow 4$
610.7(1)	1.0(1)				$12^+ \rightarrow$		$3 \rightarrow$
613.0(1)	72.7(22)	56.3(17)	0.94(3)		$11^- \rightarrow 10^-$	$M1/E2$	1
640.6(1)	2.8(1)	0.9(1)			$10^- \rightarrow 10^-$	$M1/E2$	$4 \rightarrow 1$
646.6(1)	1.9(1)				$(19^+) \rightarrow (18^+)$	$M1/E2$	$\rightarrow 3$
669.3(1)	1.1(1)	0.6(1)			$11^{(-)} \rightarrow (10^-)$	$M1/E2$	$5 \rightarrow$
681.5(10)	0.6(1)	0.7(1)			$(9^+) \rightarrow 8^+$	$M1/E2$	6
695.1(1)	1.1(1)				$(20^+) \rightarrow (19^+)$	$M1/E2$	
708.2(1)	2.1(1)				$(22^+) \rightarrow (21^+)$	$M1/E2$	3
713.8(1)	2.8(2)	2.9(2)			$(10^+) \rightarrow (9^+)$	$M1/E2$	6
714.5(1)	4.8(10)	10.7(13)			$8^+ \rightarrow 7^+$	$M1/E2$	$6 \rightarrow 1$
732.3(2)	0.8(1)	0.8(1)			$(10^-) \rightarrow (9^+)$	$E1$	$\rightarrow 6$
733.4(1)	1.1(1)	0.9(1)	1.19(37) ⁱ		$(12^-) \rightarrow 11^-$	$M1/E2$	$7 \rightarrow 1$
736.8(1)	2.6(1)	1.1(1)	0.84(13) ⁱ		$17^- \rightarrow 16^-$	$M1/E2$	2
740.2(1)	1.5(1)				$(18^+) \rightarrow (17^+)$	$M1/E2$	$\rightarrow 3$
744.2(2)	0.8(1)	0.8(1)			$(11^+) \rightarrow (10^+)$	$M1/E2$	6
748.4(1)	1.0(1)	0.2(1)			$(18^+) \rightarrow (17^+)$	$M1/E2$	$8 \rightarrow 3$
753.0(1)	2.6(2)	2.2(1)			$(14^-) \rightarrow 12^-$	$E2$	$\rightarrow 4$
753.6(7)	0.4(1)	0.2(2)			$10^- \rightarrow 8^-$	$E2$	1
754.3(2)	0.6(1)	0.3(1)			$(18^+) \rightarrow (17^+)$	$M1/E2$	$\rightarrow 3$
766.9(1)	1.0(1)				$(23^+) \rightarrow (22^+)$	$M1/E2$	3
769.1(1)	1.5(1)	1.1(1)			$(16^-) \rightarrow (14^-)$	$E2$	
799.7(1)	27.0(11)	35.3(14)	2.04(10)	1.31(29)	$7^- \rightarrow 7^+$	$E1$	1
805.3(2)	1.8(1)	1.8(1)			$10^- \rightarrow (9^+)$	$E1$	$4 \rightarrow 6$
808.0(1)	54.0(17)	58.2(19)	0.96(3)	0.67(15)	$8^- \rightarrow 7^+$	$E1$	1
809.9(1)	3.3(2)	3.0(2)			$8^- \rightarrow 8^-$	$M1/E2$	$4 \rightarrow 1$
815.0(1)	7.0(2)	2.8(1)	1.30(32)		$16^- \rightarrow 15^-$	$M1/E2$	2
817.4(1)	4.9(2)	4.9(2)		1.03(23)	$8^- \rightarrow 7^-$	$M1/E2$	$4 \rightarrow 1$
825.4(2)	1.1(1)	0.8(1)			$9^{(-)} \rightarrow (9^+)$	$E1$	$5 \rightarrow 6$
830.6(1)	11.6(4)	8.9(3)		1.12(12)	$13^{(-)} \rightarrow 11^{(-)}$	$E2$	5
855.9(1)	1.6(1)				$(17^+) \rightarrow 15^+$	$E2$	3
878.0(1)	8.3(3)	8.4(3)	1.72(35)	0.93(17)	$12^- \rightarrow 10^-$	$E2$	4
881.3(1)	5.3(2)	3.9(1)	1.61(39)	0.79(15)	$18^- \rightarrow 16^-$	$E2$	4
889.1(1)	7.8(3)	5.0(2)			$19^{(-)} \rightarrow 17^{(-)}$	$E2$	5
937.1(1)	4.2(2)	2.6(1)			$(20^-) \rightarrow 18^-$	$E2$	4
946.2(1)	6.4(2)	3.1(1)		0.92(12) ^j	$21^{(-)} \rightarrow 19^{(-)}$	$E2$	5
950.4(1)	9.1(3)	7.5(2)		0.92(12) ^j	$17^{(-)} \rightarrow 15^{(-)}$	$E2$	5
955.3(1)	6.4(2)	4.7(2)	0.88(21)		$13^+ \rightarrow 12^-$	$E1$	$3 \rightarrow$
977.0(1)	10.4(4)	8.1(3)			$15^{(-)} \rightarrow 13^{(-)}$	$E2$	5
981.7(1)	1.2(1)				$(17^-) \rightarrow (15^-)$	$E2$	
1024.3(1)	6.0(2)	4.6(2)		0.96(12)	$16^- \rightarrow 14^-$	$E2$	4
1035.6(1)	5.5(2)	4.5(2)	1.69(41)		$12^- \rightarrow 10^-$	$E2$	$2 \rightarrow 1$
1046.1(1)	2.7(2)	1.3(1)			$(11^-) \rightarrow 10^-$	$M1/E2$	$7 \rightarrow 1$
1052.3(1)	1.5(1)				$(18^+) \rightarrow 16^+$	$E2$	3
1070.1(1)	1.1(1)	0.5(1)			$11^{(-)} \rightarrow 11^-$	$M1/E2$	$\rightarrow 1$
1072.0(1)	4.2(2)	1.0(1)			$(23^-) \rightarrow 21^{(-)}$	$E2$	5

TABLE IV. (*Continued.*)

E_γ (keV)	$I_{\gamma,thin}$	$I_{\gamma,backed}$	$R_{DCO}(D)$	$R_{DCO}(Q)$	$I_i^\pi \rightarrow I_f^\pi$	$M\lambda$	Band
1076.5(1)	8.1(3)	6.3(2)		1.01(12) ^k	$14^- \rightarrow 12^-$	$E2$	4
1077.6(2)	0.8(1)				$13^{(+)} \rightarrow 13^-$	$E1$	8→2
1078.1(1)	3.3(4)	2.6(3)		1.01(12) ^k	$(10^-) \rightarrow 8^-$	$E2$	→1
1088.6(1)	2.0(1)	0.7(1)			$(22^-) \rightarrow (20^-)$	$E2$	4
1102.2(1)	2.4(1)				$(15^+) \rightarrow 14^+$	$M1/E2$	→3
1105.0(1)	2.0(1)	0.9(1)			$14^+ \rightarrow 13^-$	$E1$	3→2
1111.2(2)	1.5(1)	0.8(1)			$(10^-) \rightarrow 9^-$	$M1/E2$	→1
1115.9(1)	1.1(1)	0.7(1)			$11^{(-)} \rightarrow (10^-)$	$M1/E2$	
1122.7(1)	1.4(1)	1.0(1)	1.02(28) ⁱ		$13^+ \rightarrow 12^-$	$E1$	3→2
1130.9(2)	1.0(1)				$(15^-) \rightarrow 14^-$	$M1/E2$	→2
1138.6(2)	0.9(1)				$(19^+) \rightarrow (17^+)$	$E2$	3
1157.0(1)	8.3(3)	8.1(3)			$11^- \rightarrow 9^-$	$E2$	1
1178.3(2)	0.8(1)	0.3(1)			$15^{(+)} \rightarrow 14^-$	$E1$	8→2
1183.2(3)	0.7(1)	0.7(1)			$10^- \rightarrow 9^-$	$M1/E2$	4→1
1196.4(2)	1.9(2)				$(13^-) \rightarrow 11^-$	$E2$	→1
1202.3(2)	1.3(1)	1.0(1)			$9^{(-)} \rightarrow 9^-$	$M1/E2$	5→1
1203.2(1)	2.0(1)	1.7(1)			$12^- \rightarrow 10^-$	$E2$	→1
1230.5(1)	4.2(2)	2.3(1)			$13^{(-)} \rightarrow 12^-$	$M1/E2$	9→
1234.9(1)	2.5(1)	0.3(1)			$(25^-) \rightarrow (23^-)$	$E2$	5
1243.8(1)	5.3(2)	3.8(1)	0.87(15)		$14^{(+)} \rightarrow 13^-$	$E1$	8→2
1257.3(1)	1.9(2)	1.2(1)			$(10^-) \rightarrow 9^-$	$M1/E2$	7→1
1290.7(5)	1.1(2)	1.3(2)			$(10^+) \rightarrow (9^+)$	$M1/E2$	→6
1310.4(2)	1.0(1)				$(24^-) \rightarrow (22^-)$	$E2$	4
1318.0(1)	5.0(2)	2.6(1)	0.93(19)		$13^{(+)} \rightarrow 12^-$	$E1$	8→2
1321.2(1)	2.7(2)	3.2(2)			$(10^-) \rightarrow 8^-$	$E2$	→1
1337.7(1)	15.8(5)	9.9(3)	1.22(20)		$12^+ \rightarrow 11^-$	$E1$	3→1
1346.5(2)	1.5(1)	1.6(1)			$(12^-) \rightarrow 10^-$	$E2$	7→1
1370.1(1)	1.4(1)	0.4(1)			$15^{(-)} \rightarrow 14^-$	$M1/E2$	9→2
1396.4(1)	2.5(7)	4.2(9)			$(9^+) \rightarrow 7^+$	$E2$	6→1
1419.1(1)	1.2(1)				$(27^-) \rightarrow (25^-)$	$E2$	5
1425.6(2)	1.0(1)	0.4(1)			$14^{(-)} \rightarrow 13^-$	$M1/E2$	9→2
1467.5(1)	2.2(2)	1.5(2)			$(10^-) \rightarrow 8^-$	$E2$	7→1
1522.6(1)	1.3(1)	0.5(1)			$12^{(-)} \rightarrow 11^-$	$M1/E2$	9→1
1552.0(2)	0.9(1)	0.2(1)			$17^- \rightarrow 15^-$	$E2$	2
1589.9(1)	3.0(2)	1.9(1)			$(11^-) \rightarrow 9^-$	$E2$	7→1
1590.2(3)	0.5(1)				$(19^+) \rightarrow (18^+)$	$M1/E2$	→3
1617.0(4)	0.6(1)	2.4(1)			$8^- \rightarrow 7^+$	$E1$	4→1
1626.8(6)	0.2(1)				$(29^-) \rightarrow (27^-)$	$E2$	5
1684.1(5)	0.2(1)	0.1(1)			$11^{(-)} \rightarrow 10^-$	$M1/E2$	→1
1690.2(2)	0.8(1)	0.4(1)			$(17^-) \rightarrow 15^-$	$E2$	→2
1750.0(3)	0.8(1)				$(16^-) \rightarrow 14^-$	$E2$	→2
1765.5(1)	0.8(1)	0.5(1)			$11^+ \rightarrow 10^-$	$E1$	3→1

^aTransition not observed, but inferred from coincidence relationships.

^b R_{DCO} from gate on 285-keV dipole transition.

^c R_{DCO} from gate on 289-keV dipole transition.

^d R_{DCO} from gate on 224-keV dipole transition.

^eFit to composite ~289-keV peak.

^fFit to composite ~297-keV peak.

^g R_{DCO} from gate on 808-keV pure dipole transition.

^h R_{DCO} from summed gate on 808- and 210-keV dipole transitions.

ⁱ R_{DCO} from summed gate on 808-, 210-, and 544-keV dipole transitions.

^jAs a result of Doppler broadening, the 946- and 950-keV transitions could only be fitted as a composite peak.

^kFit to composite ~1077-keV peak.

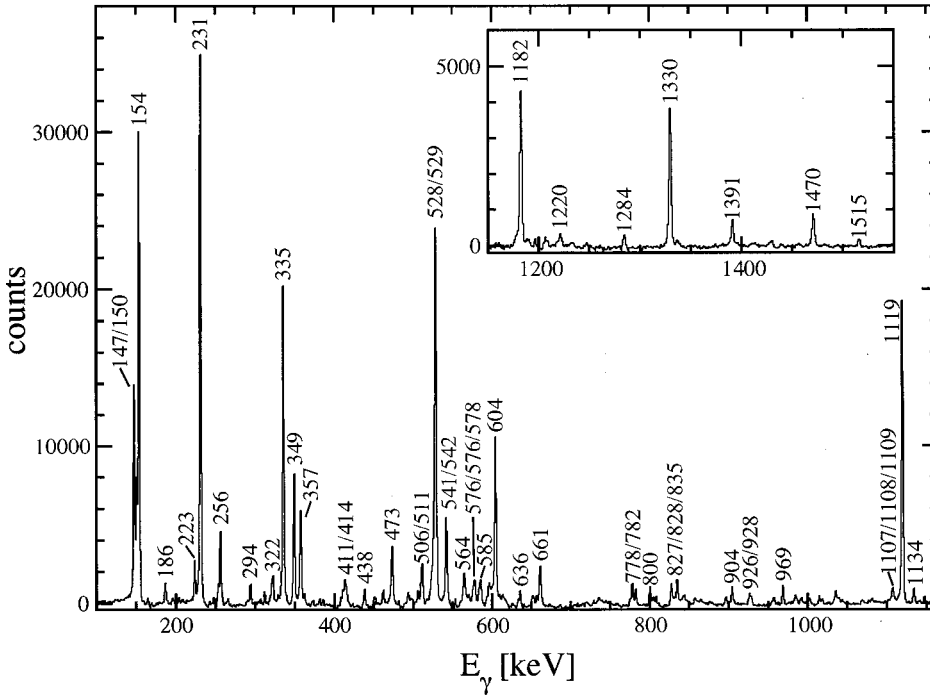


FIG. 4. Background-subtracted spectrum gated on the 213-keV transition in the ^{108}In backed-target data. Peaks associated with ^{108}In are labeled with their energies in keV.

Uncertainty with respect to the number of ~ 578 - and ~ 529 -keV transitions complicates the DCO analysis of these transitions. The 1861-keV transition is in coincidence with the 578-keV transition, but not the (tentative) 577-keV

transition. By gating on 578 keV, measuring R_{DCO} for 1861 keV, and comparing the result with the R_{DCO} values obtained for 1861 keV by gating on 778 or 835 keV, the in-band 578-keV γ ray has been shown to be consistent with stretched $E2$ multipolarity. Thus, the 2439-keV state in band 4 is proposed to have $I^\pi = 10^{(-)}$. The only other transition feeding out of this $10^{(-)}$ state for which R_{DCO} could be measured is the 1043-keV γ ray feeding band 8; this transition is consistent with pure $\Delta I = 1$ multipolarity and, hence, with the assigned spins in both bands (see Sec. IV A 6).

Gates on the 835- or 778-keV γ rays yield R_{DCO} values consistent with $E2$ multipolarity for the 992-, 553-, 904-, and 1002-keV in-band γ rays and the 928- and 804-keV side band γ rays. The 1109-, 613-, and 1179-keV γ rays were too weak to measure R_{DCO} ratios. While there are no strong gates that isolate the 828-keV member of the ~ 828 -keV doublet in band 5, gating on just the 804- and 928-keV transitions associated with band 5 isolates the 827-keV member linking bands 4 and 5 for separate measurement. The resulting DCO ratio was consistent with pure stretched dipole multipolarity. Stretched $E2$ multipolarity can be assigned to the other 828-keV γ ray based on the stretched $E2$ multiplicities of the 904-, 928-, and 804-keV transitions. Hence, band 4 has been assigned negative parity and signature $\alpha = 0$, and band 5 has been assigned $\alpha = 1$.

5. Band 7

Band 7 was found in this study to have a 223-322-414-keV γ -ray sequence, in agreement with band 1 of Ref. [24]. The 511- and 626-keV transitions placed at the top of the band in the previous work, however, have instead been placed feeding out from the level at 2879 keV which is directly fed by the 223-keV transition. The 626-keV γ ray was observed to be in coincidence with the 237-keV γ ray in band 8, but the 511-keV γ ray was not. The 506-, 1035-, and

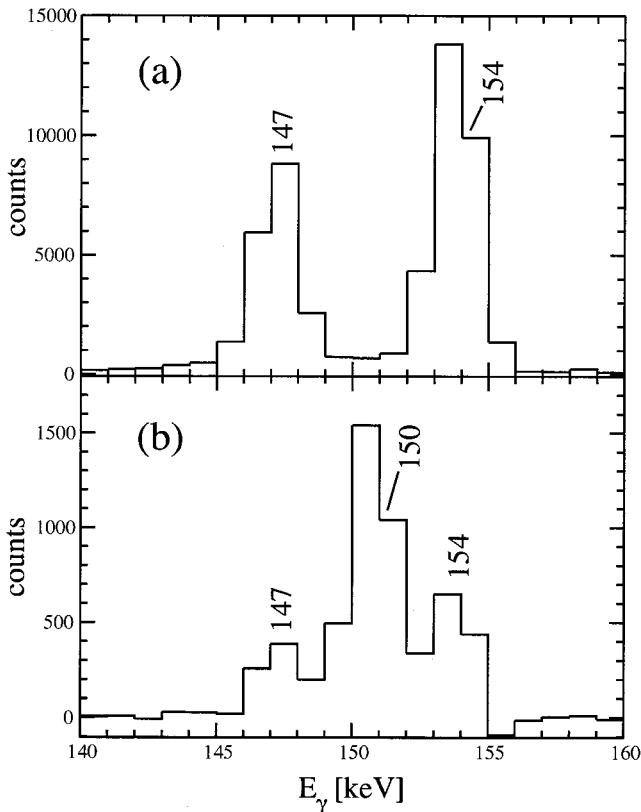


FIG. 5. Background-subtracted spectra gated on the (a) 1119- and (b) 969-keV transitions in the ^{108}In backed-target data. Peaks are labeled with their energies in keV.

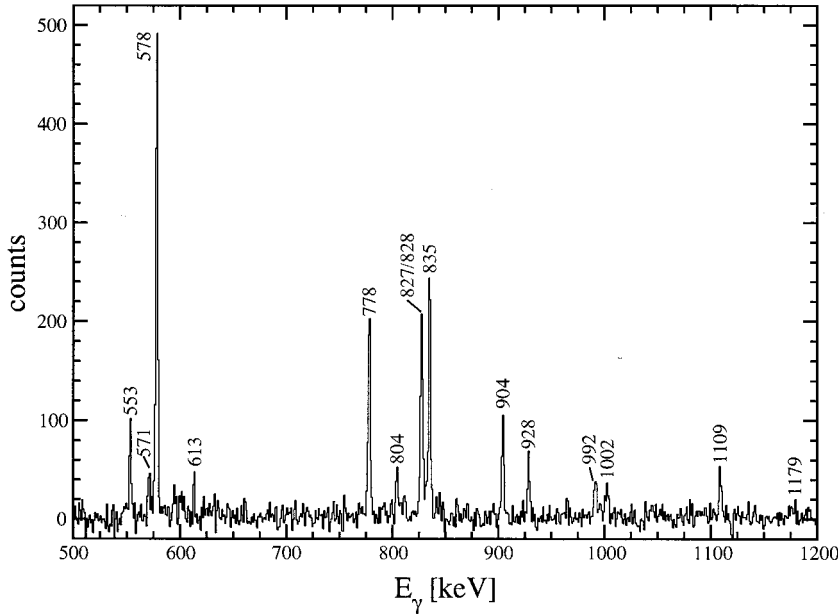


FIG. 6. Background-subtracted spectrum gated on the 1861-keV transition in the ^{108}In backed-target data. Peaks are labeled with their energies in keV.

1249-keV transitions feeding into band 1 firmly establish the existence of the level at 2368 keV, which is directly fed by the 511-keV γ ray. This level is also fed by the 294-keV γ ray feeding out of band 2. These three transitions feeding band 1 are in coincidence with band 7 and the 511-keV transition, but not with the 626-keV transition. The 511- and 626-keV γ rays, therefore, feed out of band 7 through parallel decay paths.

The highly fragmented nature of the decay of band 7 unfortunately hinders resolution of all the decay paths. The 626-keV transition feeds band 8, but the full decay path could not be established; and likewise for the 290-keV transition feeding band 1 from the state at 2368 keV. Several other γ rays, with energies 1469, 972, and 805 keV, were observed to link bands 7 and 8.

The measured R_{DCO} values for the 223-, 322-, and 414-keV transitions suggest $\Delta I=1$ mixed $M1/E2$ multipolarity for these transitions. The R_{DCO} values for the transitions with energies 294 (from band 2), 506, 511, and 1018 keV were measured; the DCO ratios for the 294- and 511-keV transitions are consistent with $\Delta I=1$ mixed $M1/E2$ multipolarity, but the uncertainties for the other two transitions are too large to permit any reliable conclusions to be drawn. Based on the R_{DCO} value for the 294-keV γ ray, the spin of the 2368-keV state is deduced to be $I=10$. This state feeds the 8^- , 9^- , and 10^- states of band 1. Only an $E2$ multipolarity for the 1249-keV transition is consistent with the parallel branches, so the state at 2368 keV is assigned $I^\pi = 10^-$. As the in-band transitions of band 7 are all consistent with $\Delta I=1$ mixed $M1/E2$ assignments, band 7, therefore, has negative parity and spins as shown in Fig. 2.

6. Band 8

The sequence of γ rays labeled band 8 decays to the 7^+ ground state via paths parallel to the 1119- and 213-keV transitions. The current analysis extends the sequence re-

ported in Ref. [24] by the addition of a 1344-keV γ ray feeding into the top level of the sequence, a 1246-keV γ ray feeding out to the 7^+ state at 150 keV, and 972- and 805-keV γ rays linking bands 7 and 8. Also, a 589-keV γ ray is observed feeding into the 8^+ state at 808 keV, which provides further confirmation of the ordering of the 656- and 749-keV transitions of band 6.

An earlier study of ^{108}In [22] proposed the assignment of the 1397- and 237-keV transitions to ^{108}In on the basis of an excitation function. These transitions were suggested to be part of the decay of an isomeric state with a lifetime on the order of $\tau \sim 100$ ns; an unobserved low-energy γ ray was proposed as the isomeric transition. The numerous transitions observed in this analysis to connect band 8 to the rest of the level scheme conclusively associate this sequence with ^{108}In . The full coincidence sequence indicated in Fig. 2, however, was observed only in the backed-target data. In the thin-target data, coincidences were observed for transitions above the state at 1634 keV in band 8, as well as prompt decay of bands 4 and 5 through the 1397-keV state in band 8, but no coincidences were observed across the 1634-keV state. This implies that the 1634-keV state has a lifetime sufficiently long for the nuclei recoiling from the thin target to exit the target region before this state decays, and thus the delayed γ rays are no longer directly observable by the Ge detectors. This effect does not appear in the backed-target data because the recoils stop in the Pb backing, and the delayed γ rays continue to have an unobstructed flight path to the detectors. If the isomeric state feeds the 1634-keV state via a low-energy γ ray, as proposed by Elias *et al.* [22], then the γ rays directly feeding the 1634-keV state should be in prompt coincidence with those transitions below that state, which is not the case.

There are no direct coincidences between the usual gating transitions for the DCO analysis, namely, the 1119- and 213-keV transitions, and the γ rays in band 8. To determine the

multipolarities of the band-8 transitions, gates were placed on the 1397- and 237-keV transitions of band 8. (Note that the angular-distribution and polarization measurements in Ref. [22] indicate these transitions are still anisotropic, despite any spin dealignment effects associated with the isomeric state; hence, a DCO analysis is still valid.) R_{DCO} values of those transitions, primarily γ rays associated with band 7, in coincidence with the gating transitions in both bands 1 and 8 were then measured. These DCO ratios were compared to the corresponding values when gating on the 1119- and 213-keV transitions. From these comparisons, a consistent set of spin and parity assignments could be deduced.

The level at 1397 keV is fed via a one-step transition of 972 keV from the 10^- state at 2368 keV and directly feeds the ground and 150-keV 7^+ states. The restriction of γ -ray multipolarities to mixed $M1/E2$, $E1$, or $E2$ limits the possible I^π for this level to 8^- or 9^+ . The gate on 237 keV yielded R_{DCO} values for band-7 transitions that were sufficiently far from those measured with gates on 213 and 1119 keV to rule out pure dipole multipolarity for the 237-keV transition. The R_{DCO} value for the 1397-keV transition when gating on 237 keV (or vice versa) indicates that the 1397-keV transition is also not pure dipole. This rules out an 8^- assignment for the 1397-keV state, resulting in a 9^+ assignment, and stretched $E2$ multipolarities for the 1397- and 1246-keV transitions, $\Delta I=1$ mixed $M1/E2$ multipolarity for the 589-keV transition, and stretched $E1$ multipolarity for the 972-keV transition. All of these assignments are consistent with the corresponding measured R_{DCO} values. With an $E2$ assignment for the 237-keV γ ray, the state at 1634 keV has $I^\pi=11^+$. Consequently, this makes the 1028-keV γ ray connecting bands 2 and 8 a nonstretched $E1$, as opposed to an $M2$ as in Ref. [24], which is consistent with R_{DCO} values measured when gated either below, on 237 keV, or above, on 231 keV. The R_{DCO} value measured for the 1469-keV γ ray connecting bands 7 and 8 is in reasonable agreement with $E1$ multipolarity, confirming the relative spins and parities of the bands.

The $E2$ assignment for the 237-keV transition is sensible in light of the observed isomeric behavior. The Weisskopf estimate for a 237-keV $E2$ transition with no collective enhancement gives a lifetime of about $\tau=35$ ns, which is sufficient for a $\beta\approx 2.9\%$ recoil to traverse the target region. With a lifetime as large as $\tau\sim 100$ ns, on the other hand, a loss of intensity through the 1634-keV state would be expected in the backed-target data since the Stony Brook array uses a 50-ns Ge-signal prompt coincidence overlap; no such loss of intensity is apparent in these data. These results provide a rough estimate of the upper and lower limits of the lifetime of this state.

B. ^{110}In level scheme

High-spin states in the nucleus ^{110}In had been studied previously by Béraud *et al.* [25]. The level scheme deduced in that work consisted primarily of three sequences of dipole transitions extending to approximately $18\hbar$. The current study extends the ^{110}In level scheme considerably, both by

the addition of new bands and the extension of the known sequences (labeled 1, 2, 3, and 8 in Fig. 3) to higher spin. Note that bands 1 and 2 were drawn as a single band in Ref. [25] but have been separated here to facilitate comparison with the results for ^{108}In . The 609-keV γ ray in the level scheme of Ref. [25] could not be confirmed, but the existence and placement of all other transitions have been confirmed. The relevant details of each band will be discussed below.

1. Bands 1 and 2

Band 1 consists of a sequence of $\Delta I=1$ transitions connecting states of negative parity, with an $I^\pi=7^-$ bandhead. The 7^- and 8^- states directly feed the 7^+ ground state and 7^+ excited state at 413 keV. Band 2 also has negative parity and, apart from the weak decay path through the 104-keV transition, exclusively feeds band 1. This work extends band 2 by the addition of the 737- and crossover 1552-keV transitions, as well as the lower-energy transitions feeding in at the top of the band.

The multipolarity of the 808-keV transition was shown to be stretched $E1$ in Ref. [25]. This pure dipole transition permitted measurements of R_{DCO} for other transitions in ^{110}In . As with ^{108}In , however, gates on energies which have higher detector efficiency than for 808 keV are more desirable. The 210-keV γ ray is unfortunately contaminated with a strong transition in ^{111}In . The 544-keV transition, which is a clean gate, has significant intensity with higher efficiency and is found to have nearly pure dipole character (see Table IV); this transition was, therefore, chosen to be the main DCO gate. Figure 7 shows a spectrum gated on 544 keV in the backed-target data. Where possible, R_{DCO} values generated by gating on 544 keV were compared with values generated by gating on 808 and 210 keV for consistency. The measured DCO ratios confirm the spins and parities of bands 1 and 2 up to $I^\pi=17^-$.

2. Band 3

Béraud *et al.* [25] observed band 3 between $12\hbar$ and $18\hbar$. Their analysis included both angular-correlation and polarization measurements of the strong 1338-keV transition connecting band 3 to negative-parity band 1; this transition was shown to have $E1$ multipolarity. Thus, band 3 has positive parity. Band 3 has been extended upwards in spin by five transitions to $23\hbar$. A 186-keV γ ray was also observed feeding out of the bottom of the band. DCO measurements confirm the I^π assignments up to 16^+ . Crossover transitions, presumed to be of $E2$ character, have been observed feeding out of the (17^+) , (18^+) , and (19^+) states. In addition to the 1338-keV γ ray, 1765-, 1123-, and 1105-keV γ rays were observed to directly feed bands 1 and 2 from the 11^+ , 13^+ , and 14^+ states of band 3, respectively. The DCO ratio of the 1123-keV γ ray is consistent with pure dipole multipolarity, although the uncertainty in the measurement is large. The $E1$ character assigned to this transition agrees with the assigned positive parity of band 3.

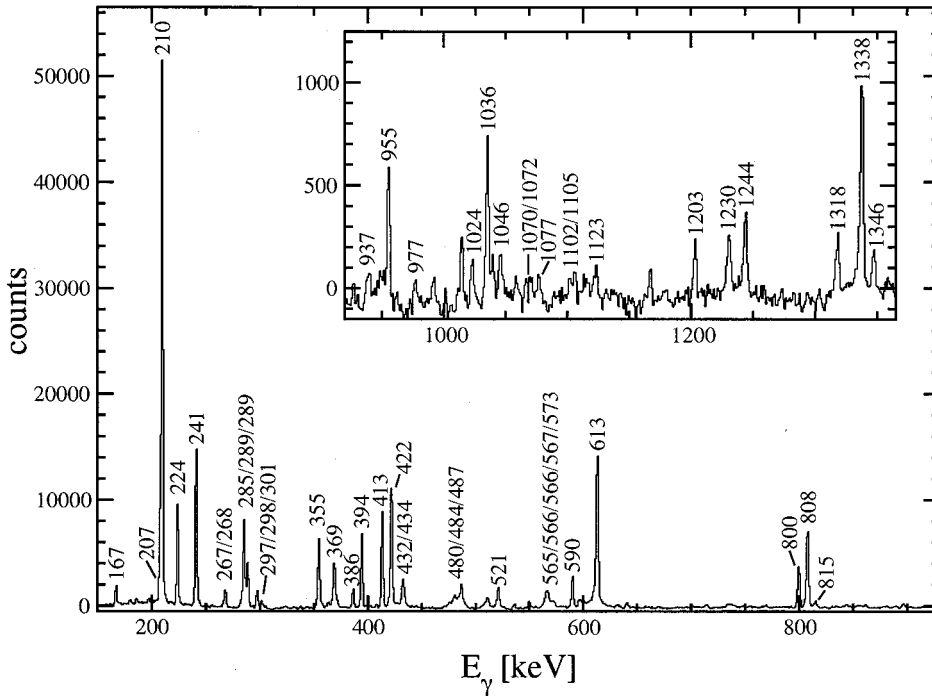


FIG. 7. Background-subtracted spectrum gated on the 544-keV transition in the ¹¹⁰In backed-target data. Peaks associated with ¹¹⁰In are labeled with their energies in keV.

3. Bands 4 and 5

The sequences labeled bands 4 and 5 in Fig. 3 have been observed for the first time in this study. Figure 8 shows summed spectra gated on (a) 878 or 1024 keV and (b) 831 or 977 keV in bands 4 and 5, respectively. The two bands are observed to high spin and do not appear to be in coincidence with each other or the rest of the level scheme apart from the feed-out transitions near the bottom of each band. Both bands decay predominantly to band 1 via multiple paths, unambiguously determining the relative excitation energies of bands 4 and 5. The transitions in these bands have been ordered on the basis of their relative intensities.

To determine the multiplicities of these new transitions, gates were placed on the 878- and 977-keV transitions of bands 4 and 5, respectively. The resulting R_{DCO} values for transitions with known multipolarity, namely, the 800-, 808-, and 210-keV γ rays associated with band 1, indicated that the gating transitions were consistent with $E2$ assignments. Using these same gates, the DCO ratios for the 1077/1078- (composite), 584-, 1024-, and 881-keV transitions in band 4, and the 578- and 831-keV transitions and 950/946-keV composite peak in band 5 were all found to be consistent with $E2$ multipolarity. Two points should be noted regarding these DCO ratios. First, the 878-keV gating transition is partially

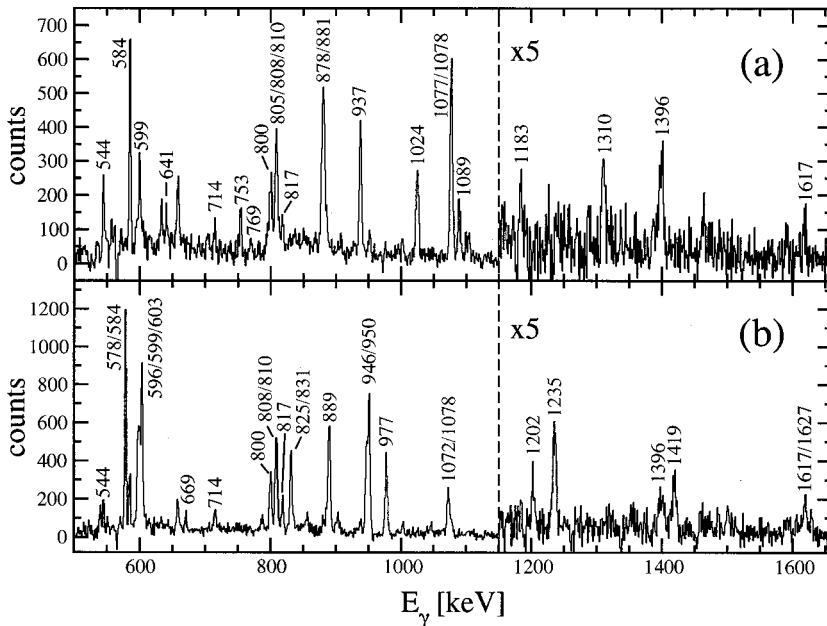


FIG. 8. Background-subtracted spectra of the summed gates on (a) 878 or 1024 keV, and (b) 831 or 977 keV in bands 4 and 5 of ¹¹⁰In, respectively, from the thin-target data. Peaks associated with ¹¹⁰In are labeled with their energies in keV.

contaminated by the in-band 881-keV transition, but since both are $E2$ transitions (as shown here), this does not affect the results of the DCO analysis. Second, the 889-keV peak for band 5 is contaminated by peaks with similar energies from neighboring nuclei and could not be isolated for a clean fit; this transition, however, as well as those higher in bands 4 and 5, are assumed to be of $E2$ character.

The DCO ratios of the transitions feeding out of the bottom of both bands were also measured in order to help establish the absolute spins and parities of the two sequences. The state at 1617 keV directly feeds the 7^- , 8^- , and 9^- states of band 1, as well as the 7^+ ground state. The DCO ratio for the 599-keV γ ray decaying to the 9^- state of band 1 rules out stretched $E2$ and pure $\Delta I=0,1$ dipole character for this transition. The remaining transitions feeding out of the 1617-keV state do not provide any more conclusive evidence for a specific I^π assignment. An $I=10$ assignment can be ruled out, however, with the assumption that the 817- and 1617-keV γ rays are not $\Delta I=3$ ($M3$ or $E3$) transitions. The only remaining possibilities are $I^\pi=8^-$ or 9^- . Comparing this nucleus with ^{108}In (see Figs. 2 and 3), there appear to be strong similarities in the decay out of ^{108}In band 4 and ^{110}In band 4. Based on these similarities, an 8^- assignment is preferred for the 1617-keV state. Band 4 is, therefore, a negative-parity band with signature $\alpha=0$ and an 8^- bandhead. The 596- and 603-keV transitions connecting bands 4 and 5 have DCO ratios consistent with pure stretched-dipole multipolarity; band 5 has been tentatively assigned negative parity based on theoretical arguments discussed in Sec. VB and has signature $\alpha=1$ and a $9^{(-)}$ bandhead.

4. Band 6

Band 6 comprises a short sequence of γ rays at low excitation energy. The 714-keV transition is self-coincident and has been placed twice in the sequence. The placement of one 714-keV γ ray feeding out of the 714-keV 8^+ state is verified by the coincidence relationships with band 1. The second 714-keV γ ray is coincident with the 1396-keV transition directly decaying to the ground state, verifying its placement above the 1396-keV state. The 714- and 744-keV γ rays are ordered by intensity.

No strong coincidences between the transitions of band 6 and transitions of known pure multipolarity have been observed, thus preventing DCO analysis. The proposed spin assignments are based on the assumption that if band 6 was a sequence of $E2$ transitions, the states of the band would be yrast and would be expected to be populated with significantly more intensity than observed in these experiments. These transitions have been assigned $\Delta I=1$ mixed $M1/E2$ multipolarity.

5. Bands 7 and 9

Bands 7 and 9 have been observed for the first time in this study. Band 7 is a sequence of four transitions which decays via multiple paths to band 1. The linking transitions between bands 1 and 7 firmly establish the ordering of the lower two transitions of band 7. The 536-keV γ ray is placed above the 289-keV γ ray based on their relative intensities.

DCO ratios for the in-band transitions of band 7 are consistent with $\Delta I=1$ mixed $M1/E2$ multipolarity. The uncertainties in the DCO ratios for those linking transitions which were measured were too large to conclusively identify them with a specific multipolarity. The proposed spins in Fig. 3 have been estimated using yrast arguments, and negative parity has been tentatively assigned based on theoretical considerations, discussed in Sec. VC.

Band 9 consists of mutually coincident 297/298-keV (doublet), 268-keV, and 434-keV γ rays. A number of high-energy transitions has been observed to connect band 9 to bands 1 and 2, firmly establishing the order of the transitions in this band. Also in coincidence with these transitions, but not with each other, are 550- and 566-keV transitions. These two transitions have been placed in parallel feeding into the top of band 9, as they are both in coincidence with the high-energy transitions feeding out of the band. The 566-keV γ ray has been assigned to be the continuation of the band based on its larger fitted intensity in the thin-target data. The 550- and 566-keV γ rays can be interchanged, however, without altering any interpretations.

The DCO ratios for the 297/298-keV composite peak, 268-keV, and 434-keV γ rays indicate $\Delta I=1$ mixed $M1/E2$ multipolarity for each. The DCO ratios for the 550- and 566-keV γ rays could not be measured, but their multipolarities are assumed to be $M1/E2$ as well. The DCO ratio for the 1230-keV γ ray is consistent with pure $\Delta I=1$ multipolarity (though with a large uncertainty), but no distinction between $M1$ and $E1$ could be made; band 9 has been tentatively assigned negative parity based on theoretical arguments discussed in Sec. VC.

6. Band 8

Band 8 in the current analysis confirms the corresponding sequence of γ rays and tentative spins up to $17\hbar$ observed in Ref. [25]. In addition to the 367-keV γ ray observed feeding into the $I=17$ member of the band, 550- and 556-keV γ rays also feeding the same state were observed. It is unclear which, if any, of these transitions is the continuation of band 8; the 550-keV γ ray has the largest intensity, however, and has been placed as part of the band. (The small difference in energies for the 550- and 556-keV transitions will not noticeably affect any conclusions drawn for this band if they are interchanged.) The 566- and 367-keV transitions, shown in Fig. 3 feeding the $I=17$ states of bands 3 and 8, respectively, were drawn in the level scheme of Ref. [25] as decaying out of two separate states. In the current analysis, these two states were found to have the same energy (within errors), and band 8 was found to be in weak coincidence with the transitions above $18\hbar$ in band 3. Thus, the two separate states in Ref. [25] have been drawn as the common $I=(18)$ state of band 3 in Fig. 3. Additional crosstalk between these bands was observed: the 748- and 754-keV transitions feed from band 8 to band 3 and the 147-keV transition feeds from band 3 to band 8 at lower spin. The DCO ratios for the strong γ rays linking bands 8 and 2, namely, the 1244- and 1318-keV γ rays, are consistent with pure stretched dipole multipolarity. The negative-parity assignment proposed by Béraud *et al.* for band 8 has, therefore,

been tentatively changed to positive, and the crosstalk between bands 3 and 8 is proposed to be due to similarities in the underlying configurations, as discussed in Secs. V A 2 and V C.

C. DSAM analysis

The data from the backed-target experiments were sorted into angle-dependent E_γ - E_γ coincidence matrices, as described in Sec. III. Gates were placed on the “all” axis of each matrix at energies corresponding to fully stopped transitions in or below each band of interest; the resulting background-subtracted coincidence spectra for various angles were projected from the matrices.

In ^{108}In , Doppler-broadened line shapes were observed for transitions above $I^\pi=13^-$ and above $I^\pi=15^+$ in the $\Delta I=1$ bands 2 and 3, respectively. Band 7 has not been extended high enough in spin to observe transitions that exhibit significant Doppler broadening. Gates near the bottom of bands 4 or 5 indicate negligible broadened line shapes for all transitions in these bands below the 1002-keV transition from the state at $21\hbar$. The lifetimes of the states high in band 5 must be sufficiently large such that the recoiling nucleus is (nearly) at rest before this cascade of transitions is emitted. This consequently prevents any meaningful line-shape analysis of these band-5 γ rays in the current study. The ramifications of the long lifetimes will be addressed in Sec. V B.

In ^{110}In , Doppler-broadened line shapes were observed for transitions above $I^\pi=13^-$ and above $I^\pi=14^+$ in the $\Delta I=1$ bands 2 and 3, respectively, and above $I^\pi=15^{(-)}$ in the $\Delta I=2$ band 5. Line shapes could not be fitted for the transitions in bands 7, 8, and 9 because of a combination of the following factors: the bands were not observed to high enough spin, were too weak, and/or had highly contaminated transitions. As with band 5 in ^{108}In , band 4 does not exhibit significant line shapes for any but the uppermost states.

For each band, background-subtracted spectra were projected from the matrices corresponding to forward, transverse, and backward angles. Lifetimes of states in each band were measured using the LINESHAPE analysis codes of Wells and Johnson [21]. These codes were used to generate 5000 Monte Carlo simulations of the velocity history of recoiling nuclei traversing the target and backing material in time steps of 0.002 ps. Electronic stopping powers were taken from the shell-corrected tabulations of Northcliffe and Schilling [26]. The number of time steps for each history was determined internally by the code as the time required for the kinetic energy of the simulated recoil to decrease to 0.1% of its initial value. Velocity profiles (components of recoil velocities in designated directions) were generated for each angle based on the detector geometry.

Typically, accurate values for the energies of the in-band transitions and side-feeding intensities would be obtained from fits to thin-target data using the same reaction, where Doppler corrections can be made. Such a procedure was followed for the ^{110}In analysis. For the ^{108}In analysis, however, different reactions were used for the thin- and backed-target experiments in the interest of channel cross section. These two reactions may feed the high-spin states with different

intensities. Thus, the energies and intensities were estimated from the backed-target data for ^{108}In by the following method: First, gates were placed below the transitions of interest, and spectra were projected from the backed-target symmetrized E_γ - E_γ matrix. Then the total counts in the broadened peak were summed for each transition, corrected for the relative detection efficiency at that energy, and normalized to the fitted intensity of a stopped transition lower in the sequence. These energy and intensity values were used as input parameters for the line-shape analysis.

Side feeding into each level and feeding into the topmost level of each band was initially modelled as a five-transition cascade with a moment of inertia fixed to be comparable to that of the in-band sequence. The quadrupole moments of the side-feeding sequences were allowed to vary; when combined with the moment of inertia, this acted as effective side-feeding lifetime parameters for each level. Once a reasonable set of initial parameters was fitted, the side feeding was changed to sequences of γ rays with independently variable lifetimes instead of a single quadrupole moment for the entire side-feeding sequence. One exception to this method is for the fitted states in band 2 of ^{108}In which are directly fed from band 3; for these states, the lifetimes determined for the feeding transitions were incorporated into the side-feeding lifetime, in addition to contributions from fast, unobserved side feeding.

Starting with the topmost transition in each band, the in-band and side-feeding lifetimes, background parameters, and contaminant-peak parameters were allowed to vary. For each set of parameters, the simulated line shape was calculated and compared to the corresponding spectrum for each angle using χ^2 -minimization routines originating from the program MINUIT [27]. The forward, transverse, and backward spectra for each transition were fitted simultaneously. The best-fit background and stopped contaminant-peak parameters were then fixed, and the in-band and side-feeding lifetimes were used as an effective feeding time parameter for the next level lower in the band. Each level was added and fitted in turn, until the entire band was included in a global fit that had independently variable lifetimes for each in-band and side-feeding level. Examples of the line-shape fits for representative transitions are shown in Fig. 9. The side-feeding cascades were typically on the order of 1–3 times faster than the in-band lifetimes. Uncertainties in the lifetime measurements were derived from the behavior of the χ^2 fit in the vicinity of the minimum and include covariance of the in-band and side-feeding lifetimes. The lifetimes of the in-band states are presented in Tables V and VI. Systematic errors associated with the modeling of the stopping powers are not included in the quoted errors and may be as large as $\pm 20\%$.

For each band, $B(M1)$ and $B(E2)$ values were calculated using the relationships

$$B(M1) = \frac{0.0569}{E_\gamma^3(M1) \tau(M1)} [\mu_N^2] \quad (2)$$

and

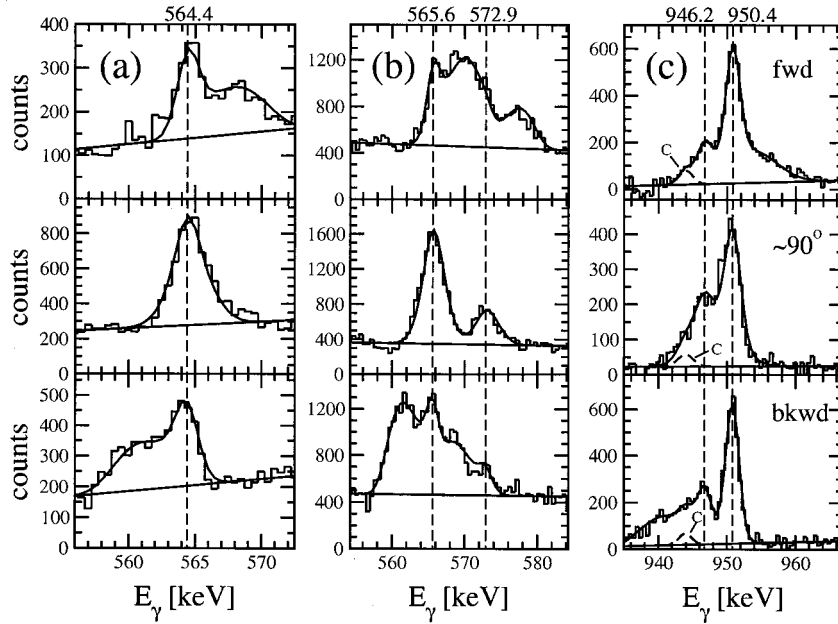


FIG. 9. Examples of line shapes from the ^{108}In and ^{110}In backed-target data. Column (a) shows the 564-keV transition in band 3 of ^{108}In , column (b) shows the 566- and 573-keV transitions in band 3 of ^{110}In , and column (c) shows the 946- and 950-keV transitions in band 5 of ^{110}In . The top, middle, and bottom rows correspond to forward, transverse, and backward detectors, respectively. The dashed vertical lines mark the stopped position of each transition. A contaminant in the spectra (c) is marked with a “C.”

$$B(E2) = \frac{0.0816}{E_\gamma^5(E2)\tau(E2)} [(eb)^2], \quad (3)$$

where the γ -ray energies E_γ are in MeV, and the partial lifetimes of the transitions $\tau(M\lambda)$, derived from the fitted lifetimes of states and observed branching ratios, are in ps. These values have been listed in Tables V and VI. Effects of internal conversion are small in each case, but have been included in the calculated values. The dipole transitions were treated as having $M1$ character with minimal $E2$ admixture ($\delta \approx 0$). For those states which have $E2$ crossovers, the corresponding $B(E2)$ values are also included in the tables. In cases where no $E2$ crossover was observed with the sensitivity in these experiments, the crossover intensity was assumed to be zero.

V. DISCUSSION

In the following discussion, band structures in both ^{108}In and ^{110}In that exhibit similar characteristics have been

grouped to facilitate interpretation of those bands. Each of the bands that has been observed to high spin in these data has been compared with self-consistent TAC model [1,11] calculations. In the calculations for the decoupled bands 4 and 5 in both ^{108}In and ^{110}In , the tilting angle θ was found to be fixed at 90° , in accordance with the $\Delta I=2$ character of these bands; in other words, principal axis cranking (PAC) solutions were found using the TAC model parametrization. For all other bands of interest ($\Delta I=1$ bands), tilted solutions with $0^\circ < \theta < 90^\circ$ were found.

Proton properties were calculated assuming zero pairing, due to the proximity of the proton Fermi surface to the $Z=50$ shell gap. As a consequence of the single-particle nature of the proton orbitals, no proton alignments are expected to occur at low frequencies. The neutron Fermi surface lies sufficiently far from the $N=50$ closed shell to warrant using a quasiparticle treatment of the neutrons. Neutron pairing constants of $\Delta_\nu = 0.85$ and 0.91 MeV were used for ^{108}In and ^{110}In , respectively, calculated as 0.8 times the experimental

TABLE V. Lifetimes of fitted states and corresponding $B(M1)$ and $B(E2)$ reduced transition strengths in ^{108}In . The $B(M\lambda)$ values have been calculated using Eqs. (2) and (3), with the lifetimes adjusted to account for branching ratios and internal conversion. Uncertainties in the lifetimes were determined from the behavior of χ^2 in the vicinity of the best-fit parameter values and were propagated through the calculation for the $B(M1)$ and $B(E2)$ strengths. These uncertainties do not include the systematic errors that are associated with the stopping powers, which may be as large as $\pm 20\%$.

Band	I_i^π	$E_{\gamma,M1}$ (keV)	$I_{\gamma,M1}$	$E_{\gamma,E2}$ (keV)	$I_{\gamma,E2}$	τ (ps)	$B(M1)(\mu_N^2)$	$B(E2)(eb)^2$
2	14^-	335.4	62.6			$1.627^{+0.056}_{-0.055}$	$0.911^{+0.032}_{-0.030}$	
	15^-	527.8	31.6	864.2	2.0	$0.603^{+0.097}_{-0.106}$	$0.600^{+0.129}_{-0.083}$	$0.017^{+0.004}_{-0.003}$
	16^-	660.9	12.7	1189.1	1.4	$0.445^{+0.024}_{-0.047}$	$0.398^{+0.046}_{-0.020}$	$0.008^{+0.001}_{-0.001}$
3	16^+	357.3	16.8			$0.432^{+0.039}_{-0.035}$	$2.48^{+0.22}_{-0.20}$	
	17^+	473.0	14.2			$0.224^{+0.017}_{-0.015}$	$2.38^{+0.17}_{-0.16}$	
	18^+	564.4	8.1	1038.8	1.3	$0.158^{+0.011}_{-0.011}$	$1.71^{+0.13}_{-0.11}$	$0.059^{+0.008}_{-0.006}$
	19^+	542.4	4.3	1107.7	1.0	$0.055^{+0.010}_{-0.018}$	$5.22^{+2.61}_{-0.83}$	$0.169^{+0.089}_{-0.029}$

TABLE VI. Lifetimes of fitted states and corresponding $B(M1)$ and $B(E2)$ reduced transition strengths in ^{110}In . The $B(M\lambda)$ values have been calculated using Eqs. (2) and (3), with the lifetimes adjusted to account for branching ratios and internal conversion. Uncertainties in the lifetimes were determined from the behavior of χ^2 in the vicinity of the best-fit parameter values and were propagated through the calculation for the $B(M1)$ and $B(E2)$ strengths. These uncertainties do not include the systematic errors that are associated with the stopping powers, which may be as large as $\pm 20\%$.

Band	I_i^π	$E_{\gamma,M1}$ (keV)	$I_{\gamma,M1}$	$E_{\gamma,E2}$ (keV)	$I_{\gamma,E2}$	τ (ps)	$B(M1)$ (μ_N^2)	$B(E2)$ ($e b$) ²
2	14 ⁻	354.6	22.2			1.252 ^{+0.035} _{-0.036}	1.006 ^{+0.029} _{-0.027}	
	15 ⁻	521.1	13.6			0.716 ^{+0.052} _{-0.042}	0.558 ^{+0.034} _{-0.038}	
3	15 ⁺	285.4	26.5			0.627 ^{+0.024} _{-0.023}	3.73 ^{+0.14} _{-0.14}	
	16 ⁺	369.0	24.4			0.428 ^{+0.008} _{-0.016}	2.61 ^{+0.10} _{-0.05}	
	(17 ⁺)	486.9	19.7	855.9	1.6	0.230 ^{+0.035} _{-0.026}	1.97 ^{+0.25} _{-0.26}	0.058 ^{+0.008} _{-0.008}
	(18 ⁺)	565.6	13.0	1052.3	1.5	0.196 ^{+0.021} _{-0.019}	1.35 ^{+0.15} _{-0.13}	0.029 ^{+0.004} _{-0.003}
	(19 ⁺)	572.9	6.2	1138.6	0.9	0.105 ^{+0.009} _{-0.013}	2.51 ^{+0.36} _{-0.20}	0.051 ^{+0.009} _{-0.005}
5	17 ⁽⁻⁾			950.4	9.1	0.774 ^{+0.105} _{-0.083}		0.136 ^{+0.016} _{-0.016}
	19 ⁽⁻⁾			889.1	7.8	0.554 ^{+0.063} _{-0.041}		0.265 ^{+0.021} _{-0.027}
	21 ⁽⁻⁾			946.2	6.4	0.403 ^{+0.023} _{-0.018}		0.266 ^{+0.013} _{-0.015}
	(23 ⁻)			1072.0	4.2	0.205 ^{+0.018} _{-0.014}		0.281 ^{+0.021} _{-0.023}

even-odd mass difference for these nuclei. The neutron chemical potential λ_n was chosen in each case such that, at $\omega=0$, the particle numbers of $N \approx 59$ and 61 were reproduced for ^{108}In and ^{110}In , respectively. The coupling constant κ for the quadrupole-quadrupole interaction used in these calculations was taken from Ref. [2] to be $\kappa = 0.036 \text{ MeV}/a^2$, where $a = 1.011A^{1/3} \text{ fm}$.

In the calculations for all configurations of neutrons and protons, the deformation parameters ε_2 and γ were chosen (to within 0.01 and 5° , respectively) such that the total energy of the nucleus in the intrinsic frame was minimized over the rotational frequency range of interest. These parameters and configurations are tabulated in Table VII. The lowest-

energy neutron orbitals involved in alignments and some configurations are labeled with the following letter scheme: A, B, \dots represent the positive-parity orbitals and E, F, \dots represent the negative-parity orbitals, in order of increasing energy.

One note should be made about the TAC calculations. TAC is an approximate, static model which treats single-particle angular momenta as if they have good projections on both the axis of symmetry of the nuclear shape and the axis perpendicular to the symmetry axis. This approximation does not account for the quantum-mechanical fluctuations of the angular momentum vectors involved. When the lengths of these vectors are small, the fluctuations may have a signifi-

TABLE VII. Summary of proposed configurations in ^{108}In and ^{110}In . The equilibrium deformation parameters indicated in columns 3 and 5 were determined at the representative rotational frequencies listed in columns 4 and 6.

Band	Configuration	^{108}In		^{110}In	
		ε_2, γ	ω (MeV/ \hbar)	ε_2, γ	ω (MeV/ \hbar)
1	$\pi[(g_{9/2})^{-1}] \otimes \nu[h_{11/2}]$	0.11, 10°	0.25	0.11, 10°	0.25
2	$\pi[(g_{9/2})^{-1}] \otimes \nu[(g_{7/2}/d_{5/2})^2 h_{11/2}]$	0.09, 15°	0.40	0.08, 10°	0.40
3 ^a	$\pi[(g_{9/2})^{-1}] \otimes \nu[(g_{7/2}/d_{5/2})(h_{11/2})^2]$	0.12, 10°	0.40	0.11, 10°	0.40
3 ^b	$\pi[(g_{9/2})^{-1}] \otimes \nu[(g_{7/2}/d_{5/2})^3 (h_{11/2})^2]$	0.06, 15°	0.60	0.08, 20°	0.60
4 ^a	$\pi[(g_{9/2})^{-2} d_{5/2}] \otimes \nu[h_{11/2}]$	0.20, 0°	0.40	0.18, -10°	0.30
4 ^b	$\pi[(g_{9/2})^{-2} d_{5/2}] \otimes \nu[(h_{11/2})^3]$			0.17, -5°	0.55
5 ^a	$\pi[(g_{9/2})^{-2} g_{7/2}] \otimes \nu[h_{11/2}]$	0.17, 5°	0.25	0.20, 0°	0.20
5 ^b	$\pi[(g_{9/2})^{-2} g_{7/2}] \otimes \nu[(h_{11/2})^3]$	0.18, 5°	0.50	0.18, 5°	0.60
6 ^a	$\pi[(g_{9/2})^{-1}] \otimes \nu[g_{7/2}]$				
6 ^b	$\pi[(g_{9/2})^{-1}] \otimes \nu[(g_{7/2}/d_{5/2})^3]$				
7	$\pi[(g_{9/2})^{-1}] \otimes \nu[(g_{7/2}/d_{5/2})^2 h_{11/2}]$ (ABF)			0.08, 0°	0.40
8 ^c	$\pi[(g_{9/2})^{-1}] \otimes \nu[(g_{7/2}/d_{5/2})(h_{11/2})^2]$ (BEF)			0.12, 10°	0.35
9 ^c	$\pi[(g_{9/2})^{-1}] \otimes \nu[(h_{11/2})^3]$			0.13, 5°	0.40

^aBelow alignment.

^bAbove alignment.

^cConfiguration assigned in ^{110}In only.

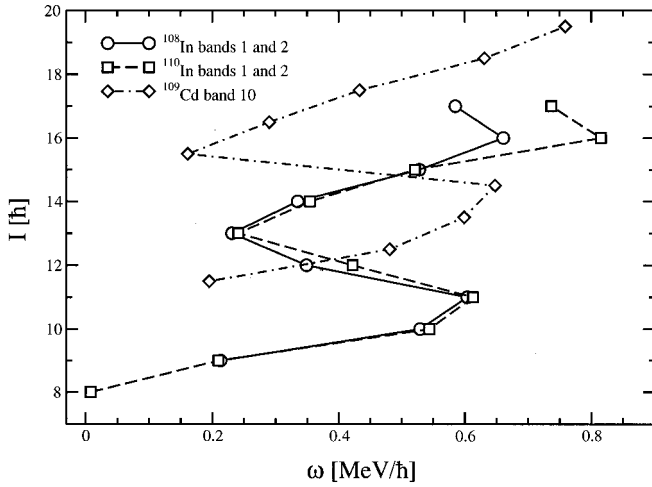


FIG. 10. Angular momentum as a function of rotational frequency for bands 1 and 2 in ^{108}In and ^{110}In and band 10 in ^{109}Cd [2].

cant effect on the calculated quantities. TAC is expected to work better for cases with large j vectors [11].

A. MR bands in $^{108,110}\text{In}$

1. $^{108,110}\text{In}$ bands 1 and 2

The observed spins I of the negative-parity $\Delta I=1$ bands 1 and 2 of $^{108,110}\text{In}$ are plotted in Fig. 10 as a function of rotational frequency ω , where $\hbar\omega(I) = E_x(I) - E_x(I-1)$. Note that in both cases, the strong $M1$ transitions connecting bands 1 and 2, at 349 and 422 keV for ^{108}In and ^{110}In , respectively, have been included on Fig. 10, and bands 1 and 2 have been drawn as a continuous sequence. For comparison, $I(\omega)$ for band 10 in an ^{110}In isotone, ^{109}Cd (as labeled in Refs. [2,28]), is also shown. This band in ^{109}Cd was interpreted as being based on the configuration $\pi[(g_{9/2})^{-2}]_{8^+} \otimes \nu[h_{11/2}]$, with the observed large backbend attributed to the alignment of the first pair of positive-parity $g_{7/2}/d_{5/2}$ neutrons, the AB alignment [2]. It is clear from Fig. 10 that all three bands show very similar behavior, including the frequencies of the observed alignments and the corresponding gains in spin. (The difference in spin between ^{109}Cd band 10 and the bands in the indium isotopes would be a consequence of the additional spin contribution from the second proton hole present for ^{109}Cd .) The bands in $^{108,110}\text{In}$ have, therefore, been interpreted as based on the $\pi[(g_{9/2})^{-1}] \otimes \nu[h_{11/2}]$ configuration for band 1 and $\pi[(g_{9/2})^{-1}] \otimes \nu[(g_{7/2}/d_{5/2})^2 h_{11/2}]$ for band 2. The assignments for band 1 in both nuclei agree with the assignments made in previous studies [22,25].

The experimental data for these bands have been compared with TAC calculations for the configurations discussed in the previous paragraph. The equilibrium deformation parameters were determined at representative frequencies for bands 1 and 2 in both isotopes and are included in Table VII. The corresponding calculated $I(\omega)$ curves are shown in Fig. 11(a) for ^{108}In and Fig. 11(b) for ^{110}In .

In both plots, the excellent agreement between experiment and theory for band 2 is apparent. The backbend observed

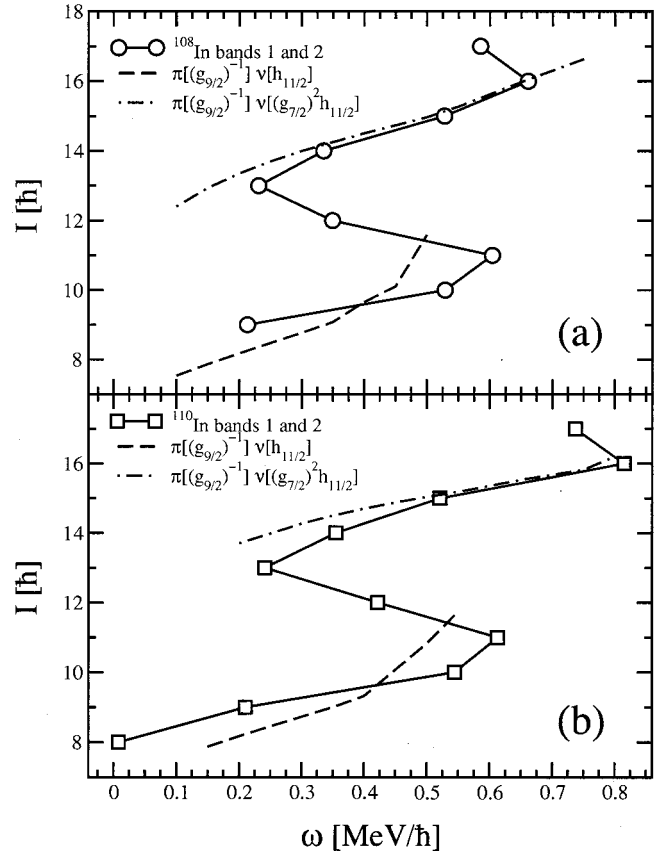


FIG. 11. Angular momentum as a function of rotational frequency for bands 1 and 2 in (a) ^{108}In and (b) ^{110}In in comparison with the corresponding TAC calculations for the assigned configurations (see Table VII). Note that the $g_{7/2}$ labels in the figure are shorthand for mixed $g_{7/2}/d_{5/2}$.

for the last point in both isotopes would correspond to a crossing with another configuration, but since the extension of this sequence falls beyond the limits of the experimental sensitivity in this analysis, no calculations were performed to attempt to reproduce this crossing.

The calculations for band 1 in either isotope are not as successful at reproducing the data as the calculations for band 2. This is likely because the static approximation used by TAC becomes more appropriate with the inclusion of a larger number of active particles and, hence, larger spin vectors. This may explain why the calculated $I(\omega)$ is improved above the alignment, in band 2.

The $B(M1)$ strengths calculated from the fitted lifetimes of states for ^{108}In band 2 are plotted as a function of frequency in Fig. 12(a). Also shown are the $B(M1)$ strengths predicted by the TAC calculations for the $\pi[(g_{9/2})^{-1}] \otimes \nu[(g_{7/2}/d_{5/2})^2 h_{11/2}]$ configuration. For this and all other TAC calculations, the intrinsic g factor used was $g_{s,eff} = fg_s$, where the spin attenuation factor f was taken to be 0.6 to roughly reproduce the experimentally observed g factors in this mass region [29].

Although the data for band 2 do not appear to show a particularly dramatic decrease in $B(M1)$ magnitude in Fig. 12(a), they do decrease by a factor of 2 over the measured range. The TAC calculation for this configuration approxi-

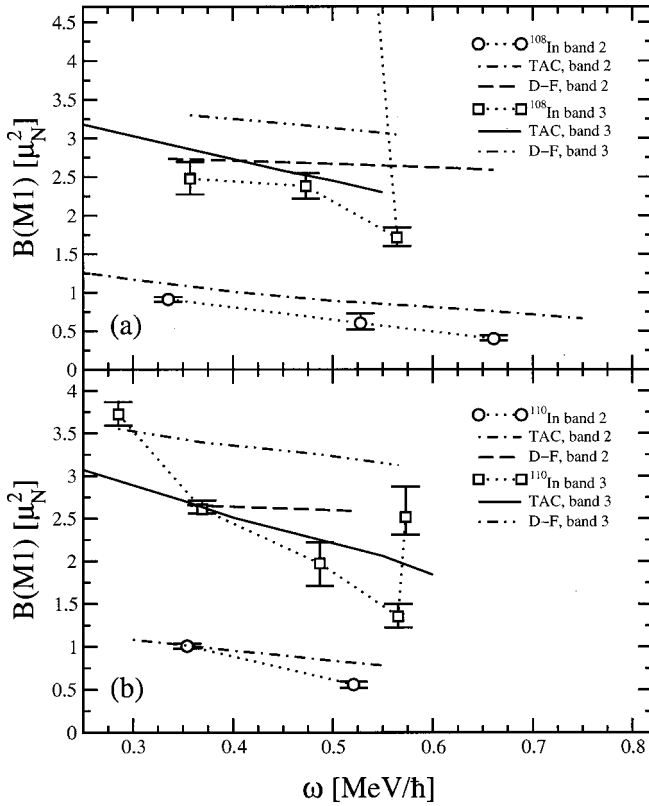


FIG. 12. Reduced $M1$ transition strength $B(M1)$ as a function of rotational frequency for bands 2 and 3 in (a) ^{108}In and (b) ^{110}In . The data points have been deduced from the fitted lifetimes (see Tables V and VI). Calculations using both TAC and the Dönau-Frauendorf fixed- K formalism (D-F) are shown for comparison. The configurations are given in Table VII.

mately reproduces the correct magnitude and slope of the data. The $B(M1)$ values were also calculated using the Dönau-Frauendorf fixed- K formalism [12]. The dashed curve shown in Fig. 12(a) was calculated assuming pure $g_{7/2}$ character for the positive-parity neutrons; including some $d_{5/2}$ admixture can have the effect of increasing the magnitude of the curve by up to about 35%. It is clear from the plot that the TAC calculation better describes the $B(M1)$ behavior than does the Dönau-Frauendorf estimate.

In band 2 of ^{110}In , only the 355-, 521-, and 815-keV transitions were sufficiently shifted and uncontaminated to perform a line-shape fit. Unfortunately, the topmost fitted state can be used only as an effective feeding lifetime for the lower states. Hence, only two transitions in this band have an associated deduced $B(M1)$ value (see Table VI); these values have been plotted in Fig. 12(b). While these data for band 2 may not fully illustrate the behavior of the $B(M1)$ strength throughout the entire band, they at least can be used to compare the relative magnitudes with the measured values for band 3 (discussed below). As for ^{108}In , the TAC and Dönau-Frauendorf predictions are plotted in Fig. 12(b). The TAC curve approximately reproduces the magnitude of the data, though with a shallower slope. TAC has significantly better agreement with the data than the Dönau-Frauendorf estimate, however. Note that, as before, the Dönau-

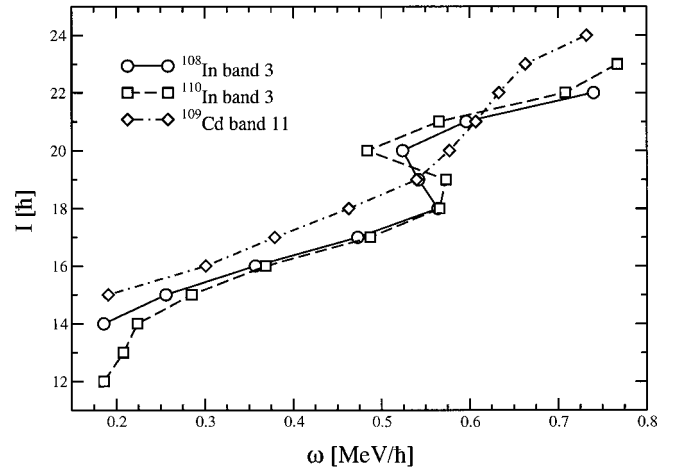


FIG. 13. Angular momentum as a function of rotational frequency for band 3 in ^{108}In and ^{110}In and band 11 in ^{109}Cd [2].

Frauendorf calculation shown involves $g_{7/2}$ character for the positive-parity neutrons, and inclusion of $d_{5/2}$ admixture increases the magnitude even further.

In addition to arguments based on $I(\omega)$ and $B(M1)$ strength, the deduced $B(E2)$ strength for crossover $E2$ transitions can also be used to compare with shears predictions. The values for the transitions in band 2 of ^{108}In (see Table V) are consistent with small deformations, comparable to those predicted by the TAC calculations for this configuration. Taking the deduced $B(E2)$ for the 528-keV transition and $\mathcal{J}^{(2)} = 7.5\hbar^2 \text{ MeV}^{-1}$ for the 15^- state yields a $\mathcal{J}^{(2)}/B(E2)$ ratio of about $450\hbar^2 \text{ MeV}^{-1} (e b)^{-2}$. This ratio is typically closer to $10\hbar^2 \text{ MeV}^{-1} (e b)^{-2}$ in nuclei described by the collective model. Hence, the shears interpretation based on the $B(M1)$ behavior for band 2 in ^{108}In is further supported by the large $\mathcal{J}^{(2)}/B(E2)$ ratio, suggesting there is a significantly larger contribution to the angular momentum from the valence high- j particles than if the band arose solely from collective rotation. No crossover $E2$ transitions were observed for the fitted levels in band 2 in ^{110}In , but this, too, indicates a small $E2$ branching ratio and a correspondingly large $\mathcal{J}^{(2)}/B(E2)$ ratio.

2. $^{108,110}\text{In}$ band 3

Band 3 in both ^{108}In and ^{110}In has been previously assigned positive parity via polarization measurements [24,25]. In Fig. 13, the spins in these two bands are plotted as a function of rotational frequency. The observed values for the positive-parity band 11 in ^{109}Cd , an $N=61$ isotone (taken from Ref. [2]), are also plotted for comparison. The general features for all three bands are similar: at low frequencies, the $I(\omega)$ curves are about the same, apart from an offset in spin due to the presence of the additional proton hole for cadmium. All of these bands exhibit a high-frequency ($\omega > 0.5 \text{ MeV}/\hbar$) alignment. This band in ^{109}Cd was shown to have the neutron configuration $\nu[(g_{7/2}/d_{5/2})(h_{11/2})^2]$, with the upbend attributed to the BC alignment [2,28]. The different appearance (sharpness) of this alignment in the isotone

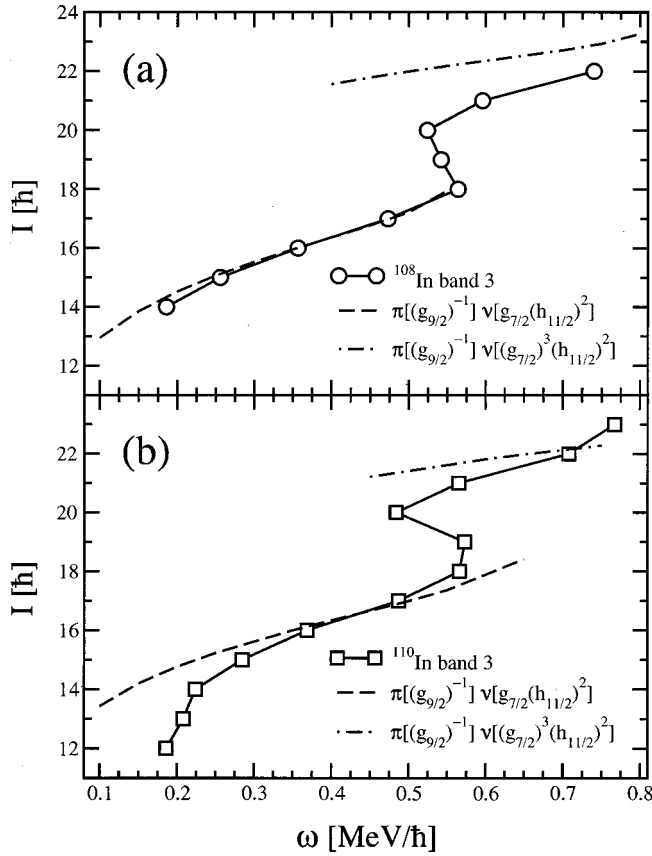


FIG. 14. Angular momentum as a function of rotational frequency for band 3 in (a) ^{108}In and (b) ^{110}In in comparison with the corresponding TAC calculations for the assigned configurations (see Table VII). Note that the $g_{7/2}$ labels in the figure are shorthand for mixed $g_{7/2}/d_{5/2}$.

^{110}In , as well as the lower alignment frequency, can most likely be attributed to a difference in the pairing Δ_p . In addition, with different proton configurations in indium and cadmium, the equilibrium tilted cranking angle θ is expected to differ, and it was found in Ref. [2] that the alignment frequencies of the positive-parity orbitals are sensitive to the value of θ . The similarity of these bands suggests that band 3 in ^{108}In and ^{110}In are based on the $\pi[(g_{9/2})^{-1}] \otimes \nu[(g_{7/2}/d_{5/2})(h_{11/2})^2]$ configuration, which becomes $\pi[(g_{9/2})^{-1}] \otimes \nu[(g_{7/2}/d_{5/2})^3(h_{11/2})^2]$ after the BC alignment.

The experimental data for band 3 in both isotopes have been compared with TAC calculations for the above configurations. The equilibrium deformation parameters were determined at representative frequencies both above and below the alignments in each band and are included in Table VII. The calculated $I(\omega)$ curves are shown in Figs. 14(a) and 14(b) in comparison with the experimental values. There is very good agreement between the data and TAC calculations for low frequencies, particularly for ^{108}In . In both cases, the theory overestimates the spin by $(1-2)\hbar$ above the alignments. This disagreement seems to be a systematic property of the $(g_{7/2}/d_{5/2})^3(h_{11/2})^2$ neutron configuration, as the overestimated spin appears in ^{108}In , ^{110}In , and ^{109}Cd . Whether this is a general difficulty related to the TAC calculations at

high frequencies, such as the treatment of pairing, or a more specific problem with the abundance of comparatively low- j , mid- Ω $g_{7/2}/d_{5/2}$ neutrons (as opposed to $h_{11/2}$ neutrons) that are active above the alignment is unclear. So far, TAC calculations in the high-frequency region have not been well explored, in part due to a shortage of available data for comparison. The pair correlations are expected to diminish with larger numbers of excited quasiparticles, whereas for these calculations the pairing parameter was kept fixed. On the other hand, the $(g_{7/2}/d_{5/2})^3$ neutron configurations proposed for band 6 in ^{108}In and ^{110}In , discussed in Sec. V D, are also not successfully reproduced with the TAC calculations, suggesting that the configuration may be a significant factor.

The $B(M1)$ transition rates deduced from the lifetime data for band 3 are plotted in Fig. 12(a) for ^{108}In and Fig. 12(b) for ^{110}In . The TAC calculations reproduce the relative $B(M1)$ magnitudes of bands 2 and 3 in both ^{108}In and ^{110}In . Furthermore, band 3 in both isotopes exhibits a decrease in $B(M1)$ magnitude with increasing spin, as expected for a shears band. The Dönau-Frauendorf estimates for the $B(M1)$ strengths for band 3 in both isotopes are also indicated by the dash-double-dotted lines in the figures. It is clear that the TAC calculations are in considerably better agreement with the data than are the Dönau-Frauendorf estimates. It should be noted that the upturn in the measured $B(M1)$ strengths occurs for the transition that is close to the alignment in each band. The behavior of the $B(M1)$ strength across alignments in a shears band was quantitatively studied for the first time for the case of ^{197}Pb [30]. Increases in $B(M1)$ strength were observed at each alignment, which can be attributed to the following process: the $B(M1)$ values decrease up to the observed alignment; when the pair of nucleons align, a new shears with longer blades forms, which results in larger $B(M1)$ strength; finally, these longer blades close as before, and the $B(M1)$ strength again decreases with spin.

The deduced $B(E2)$ strengths of the observed $E2$ cross-over transitions are listed in Table VI. The corresponding $\mathcal{J}^{(2)}/B(E2)$ ratios for states below the alignments in both bands range between 150 and $450\hbar^2 \text{ MeV}^{-1} (e b)^{-2}$, further supporting the shears interpretation for these bands.

B. AMR bands in $^{108,110}\text{In}$

In the indium isotopes, many of the bands observed to high spins are based on one intrinsic, high- Ω $g_{9/2}$ proton hole. The small signature splitting associated with this orbital results in $\Delta I=1$ bands such as those discussed in the preceding sections. The presence of decoupled bands, however, must involve low- Ω proton orbitals which have large signature splitting. These orbitals are occupied via one-particle-one-hole (1p-1h) proton excitations from the $g_{9/2}$ orbital to one of the orbitals above the $Z=50$ shell gap, namely, $\pi g_{7/2}$, $\pi d_{5/2}$, or $\pi h_{11/2}$. In order to determine the probable configurations of the observed bands in ^{108}In and ^{110}In , arguments based on systematics of the neighboring indium isotopes have been applied. In addition, PAC calculations (TAC calculations in which the tilting angle was found to be $\theta = 90^\circ$) have been performed to help support these arguments. The pair of $g_{9/2}$ proton holes will be explicitly stated

in each configuration because of their prominent role in the generation of angular momentum in AMR bands [see Fig. 1(b)].

Little is known about the $\Delta I=2$ bands in the odd-odd $A \approx 110$ indium isotopes; only one such band in ^{108}In has been published prior to the current study [24]. Based on standard cranked shell model calculations, Ref. [24] concluded that the $\Delta I=2$ band in ^{108}In exhibits the FG neutron alignment, thereby indicating there is an odd $h_{11/2}$ neutron in the configuration, and has deformation parameters $\beta_2=0.20$, $\beta_4=0.0$, and $\gamma=0^\circ$; no discussion was given regarding the proton configuration for this band. As was noted in Sec. IV A 4, however, the placement of the γ rays and the proposed spins for this band in Ref. [24] have been changed in the current analysis. This change potentially alters the interpretation.

Despite the absence of $\Delta I=2$ band systematics for the odd-odd isotopes, interpretations can still be made with use of the systematics of the neighboring odd- A indium isotopes. In Refs. [8,9], an extensive analysis of $^{107,109,111,113}\text{In}$ was performed. One feature that is apparent from that analysis is that $\Delta I=2$ bands based on a $\pi g_{7/2}$ orbital were observed in each isotope, whereas bands based on a $\pi h_{11/2}$ orbital were typically not observed down to the bandhead (as in $^{111,113}\text{In}$) or were not observed at all (as in $^{107,109}\text{In}$), because the $h_{11/2}$ proton orbital is expected to become significantly nonyrast at low rotational frequencies. The angular momenta for bands 4 and 5 in ^{108}In and ^{110}In are plotted as a function of rotational frequency in Fig. 15(a). For direct comparison with the results of the theoretical calculations for $\Delta I=2$ bands, the angular momentum is defined¹ as $I' = I - \frac{1}{2}$ and the rotational frequency is defined as $\hbar \omega(I') = \frac{1}{2} E_\gamma(I)$, where I is the spin of the observed state [11]. Shown in Fig. 15(b) are the angular momenta for two of the $\Delta I=2$ bands observed in ^{109}In (data taken from Ref. [8]). The band drawn with a dashed line in Fig. 15(b) (labeled band 2 in Ref. [8]) was proposed to have the $\pi g_{7/2}$ configuration at the bandhead and is expected to exhibit an EF neutron alignment. The other band from ^{109}In (band 9 in Ref. [8]) was proposed to involve, in addition to a positive-parity proton, the broken-pair neutron configuration $\nu[(g_{7/2}/d_{5/2})h_{11/2}]$; this blocks the EF alignment, making FG the first allowed alignment. (Note that the occurrence of any low-frequency proton alignments in these nuclei is unlikely, and the positive-parity neutron alignments occur at frequencies of about $0.55 \text{ MeV}/\hbar$ or greater at deformations ε_2 around 0.15 to 0.20. Thus, only the EF or FG neutron alignment is expected.) As indicated in Fig. 15, the alignment frequencies for both $\Delta I=2$ bands in ^{110}In are found to be very close to that observed for band 9 in ^{109}In (FG alignment). The gain in spin across the alignment for these two bands, about $(7-8)\hbar$ for each, agrees with the observed increase in the ^{109}In band 9 and is consistent with

¹The average spin is $I_{av} = \frac{1}{2}[I + (I-2)] = I-1$, and $I' = \sqrt{(I_{av})(I_{av}+1)} = \sqrt{(I-1)I}$; this is approximated as $I' \approx I - \frac{1}{2}$, which differs from the exact expression by at most 0.2% for $I > 7\hbar$.

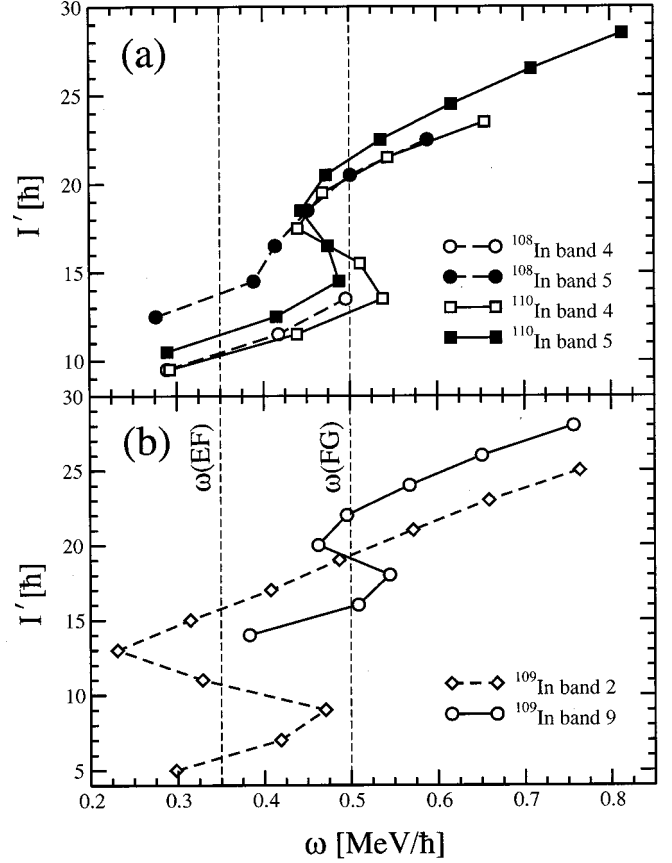


FIG. 15. Angular momentum as a function of rotational frequency for (a) the $\Delta I=2$ bands 4 and 5 in ^{108}In and ^{110}In and (b) $\Delta I=2$ bands 2 ($\pi[g_{7/2}]$) and 9 ($\pi[g_{7/2}] \otimes \nu[(g_{7/2}/d_{5/2})h_{11/2}]$) in ^{109}In (data taken from Ref. [8]). The dashed vertical lines mark the EF and FG neutron alignments in the bands in ^{109}In .

the expectation for the FG alignment. Additionally, each of these bands is observed to feed preferentially into the $\pi[(g_{9/2})^{-1}] \otimes \nu[h_{11/2}]$ band (band 1). These observations suggest that both bands 4 and 5 in ^{110}In contain an odd number of $h_{11/2}$ neutrons in their configurations.

The proton assignment for these bands can also be deduced from the level schemes. Band 4 in ^{110}In was found to have $\alpha=0$ signature, whereas band 5 has $\alpha=1$ (see Fig. 3). Signature is an additive quantum number, and since the energetically favored $h_{11/2}$ neutron has $\alpha=-1/2$, band 4 must involve a proton with $\alpha=+1/2$ and band 5 a proton with $\alpha=-1/2$. Of the low- Ω proton orbitals close to the Fermi surface, only the $d_{5/2}$ orbital has the appropriate signature for band 4, whereas either $g_{7/2}$ or $h_{11/2}$ is possible for band 5. As was noted above, however, $\pi g_{7/2}$ $\Delta I=2$ bands were observed in all of the neighboring odd- A indium isotopes, as $g_{7/2}$ is energetically favored over $h_{11/2}$ at low rotational frequencies. Also, the bandhead spin for the $\pi[(g_{9/2})^{-2}h_{11/2}] \otimes \nu[h_{11/2}]$ configuration should be $I=11$, whereas band 5 is observed down to spin $I=9$. Hence, the configurations assigned to these bands are $\pi[(g_{9/2})^{-2}d_{5/2}] \otimes \nu[h_{11/2}]$ for band 4 and $\pi[(g_{9/2})^{-2}g_{7/2}] \otimes \nu[h_{11/2}]$ for band 5, with the FG neutron alignment occurring in both. (The distinction between the two proton orbitals may not be so clear, however,

as there are possible admixtures between them.) Bands built on these configurations would be expected to have an 8^- and 9^- bandhead, respectively, consistent with the deduced level scheme.

There is no alignment in band 4 of ^{108}In over the range of spins observed in this study, thus preventing a comparison of alignment frequencies with the odd- A neighbors. Similarities in signature, proposed parity, decay, and $I'(\omega)$ between this band and band 4 in ^{110}In below the alignment, however, suggest the configuration $\pi[(g_{9/2})^{-2}d_{5/2}] \otimes \nu[h_{11/2}]$ for band 4 in ^{108}In . This configuration is consistent with the fact that there is no alignment below the maximum observed frequency in this band [refer to Fig. 15(a)] and with the observed bandhead spin.

The interpretation for band 5 in ^{108}In is not as apparent as the other $\Delta I=2$ bands discussed thus far. This band appears to have an alignment with a large interaction strength at a frequency in between the EF and FG alignment frequencies in ^{109}In . The $I'(\omega)$ curve for this band more closely matches that of band 4 in ^{110}In than band 5, although they have different values of signature quantum number. Band 5 in ^{110}In has measurable line shapes, whereas band 5 in ^{108}In has none except at the highest observed spins. These observations suggest that band 5 in ^{108}In may be based on a different configuration than that of band 5 in ^{110}In , which has been assigned $\pi[(g_{9/2})^{-2}g_{7/2}] \otimes \nu[(h_{11/2})^3]$ above the alignment. The next lowest energetically favored configuration assignment appropriate for this band in ^{108}In is the $\pi[(g_{9/2})^{-2}d_{5/2}] \otimes \nu[(g_{7/2}/d_{5/2})(h_{11/2})^2]$ configuration. Note that this configuration has positive parity, but this is still consistent with the pure-dipole multipolarity of the 827-keV transition connecting bands 4 and 5.

Cranking calculations were performed for both the $\pi[(g_{9/2})^{-2}g_{7/2}] \otimes \nu[h_{11/2}]$ and $\pi[(g_{9/2})^{-2}d_{5/2}] \otimes \nu[(g_{7/2}/d_{5/2})]$ configurations in ^{108}In and followed through the FG and EF neutron alignments, respectively. The calculated $I'(\omega)$ curves are plotted in comparison with band 5 in Fig. 16(a). The $\pi[(g_{9/2})^{-2}g_{7/2}] \otimes \nu[h_{11/2}]$ calculation successfully reproduces the observed alignment frequency (FG) and interaction strength, whereas for the $\pi[(g_{9/2})^{-2}d_{5/2}] \otimes \nu[(g_{7/2}/d_{5/2})]$ calculation, the predicted alignment, EF , falls about 0.15 MeV/ \hbar lower in frequency than the observed alignment. Hence, band 5 has been assigned the $\pi[(g_{9/2})^{-2}g_{7/2}] \otimes \nu[h_{11/2}]$ configuration, which becomes $\pi[(g_{9/2})^{-2}g_{7/2}] \otimes \nu[(h_{11/2})^3]$ above the alignment. The reason for the $(1-2)\hbar$ discrepancy in predicted spins for this band is unclear, but overall other configurations are less compatible with the observed properties. The absence of line shapes may be a consequence of longer-lived in-band states, indicating smaller deformation than for the corresponding band in ^{110}In , or slower side feeding into this band.

Calculations were also performed for comparison with the other $\Delta I=2$ bands in both isotopes (refer to Table VII); band 4 of ^{108}In is shown in Fig. 16(a) and bands 4 and 5 of ^{110}In are shown in Fig. 16(b). Three of the one-quasineutron calculations (band 4 in ^{108}In and below the alignments in bands 4 and 5 in ^{110}In) are about $(2-4)\hbar$ higher in spin than the corresponding data. Above the FG alignment in both bands

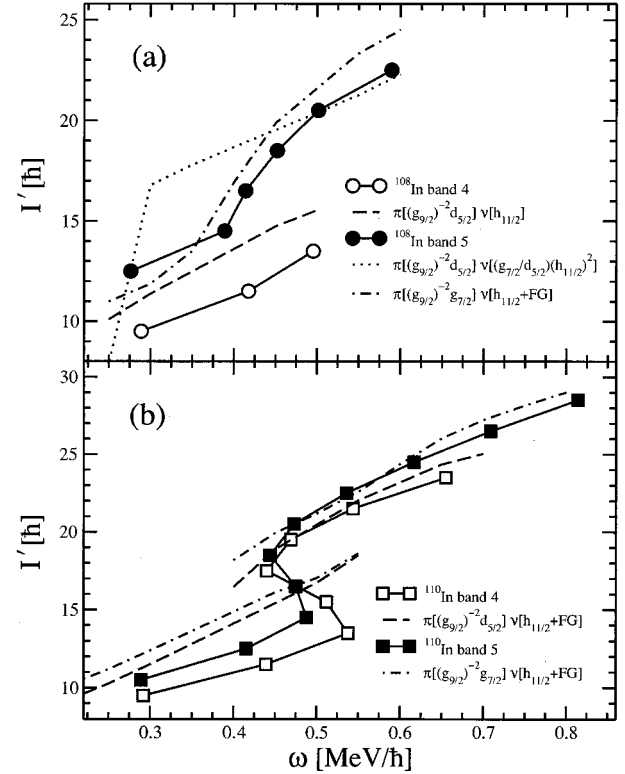


FIG. 16. Angular momentum as a function of rotational frequency for bands 4 and 5 in (a) ^{108}In and (b) ^{110}In in comparison with the corresponding PAC calculations for the assigned configurations (see Table VII). See Sec. V B regarding the two calculations for band 5 in ^{108}In . The notation $\nu[h_{11/2}+FG]$ in the legends indicates that the calculations involving $\nu[h_{11/2}]$ were continued above the FG alignment and are drawn with a common line style.

in ^{110}In , the calculations for the three-quasineutron configurations are found to successfully reproduce the data to within $1\hbar$. Similar behavior was observed in the $\Delta I=2$ band 5 in ^{109}Cd [2], which has a configuration differing from those in the indium isotopes by a $d_{5/2}$ or $g_{7/2}$ proton. This is probably an effect similar to that discussed in Sec. V A 1 for bands 1 and 2, where the TAC calculations are in better agreement with the data for configurations that have a larger number of valence particles. Unlike the other $\Delta I=2$ bands, the calculations for the lower part of band 5 in ^{108}In slightly underestimate the spin, but no strong conclusions should be drawn based on the sole state observed below the alignment. Overall, these calculations further support the proposed configuration assignments.

The $B(E2)$ strengths for the transitions in band 5 in ^{110}In for which lifetimes were measured (see Table VI) have been plotted in Fig. 17. Also shown are the $B(E2)$ values predicted by the cranking calculations for the corresponding configuration. The quadrupole deformation was found to be $\varepsilon_2 \approx 0.18$ over the frequency range of the experimental data. At frequencies $\omega > 0.70$ MeV/ \hbar , the calculated deformation becomes distinctly smaller, as do the $B(E2)$ values, but more sensitive lifetime data would be required in order to confirm this predicted effect. Note that the point at $\omega = 0.475$ MeV/ \hbar ($E_\gamma = 950$ keV) in Fig. 17 is at the align-

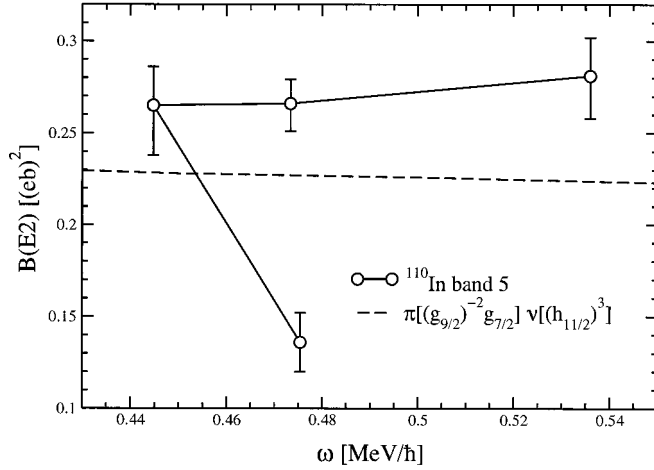


FIG. 17. Reduced $E2$ transition strength $B(E2)$ as a function of rotational frequency for band 5 in ^{110}In . The data points have been deduced from the fitted lifetimes (see Table VI). The predicted $B(E2)$ values for the given configuration are also shown for comparison.

ment and is expected to show anomalous behavior due to admixtures between the two crossing configurations. Apart from this point, the rest of the measured $B(E2)$ strengths have approximately the same magnitude, about $0.035 (e b)^2$ larger than the calculated values. By increasing ε_2 or decreasing γ slightly, by about one grid point in the calculations (0.01 and 5° , respectively), these measured values can be reproduced by the theory.

Taking $\mathcal{J}^{(2)} = 19.2\hbar^2 \text{ MeV}^{-1}$ and $70.2\hbar^2 \text{ MeV}^{-1}$ at the top of the band and just above the backbend in band 5, respectively, and the experimental $B(E2)$ strength as approximately $0.265 (e b)^2$ throughout, yields $\mathcal{J}^{(2)}/B(E2)$ ratios that vary between $72\hbar^2 \text{ MeV}^{-1}$ and $265\hbar^2 \text{ MeV}^{-1} (e b)^{-2}$. This range of values is about an order of magnitude larger than values expected for a typical deformed rotational band [$\sim 10\hbar^2 \text{ MeV}^{-1} (e b)^{-2}$ [11]]. Thus, this band satisfies one of the criteria for an AMR interpretation, although a decreasing $B(E2)$ strength needs to be demonstrated for a more conclusive interpretation.

Band 4 in ^{110}In and bands 4 and 5 in ^{108}In did not exhibit sufficiently shifted line shapes to allow any lifetimes to be measured. These bands may be good candidates for AMR. Lower limits can be placed on the lifetimes of states in each band by estimating, for the topmost measurable transition, the maximum Doppler shift possible that would fall below the experimental sensitivity in this analysis. To accomplish this, the quadrupole moments of the in-band transitions were all assumed to be equal, and the side-feeding quadrupole moments were set such that the corresponding side-feeding lifetimes were about 20% faster than the in-band transitions, as was the case for band 5 in ^{110}In . The quadrupole moments were then scaled until a distinct shifted line shape was predicted by the LINESHAPE simulations for the 904- (937-) keV transition in ^{108}In (^{110}In) that was not apparent in the data spectra. Using this rough approach, the lifetime lower limits were determined to be $\tau(904) > 1.2 \text{ ps}$ and $\tau(937) > 1.1 \text{ ps}$. These values correspond to $B(E2) < 0.09 (e b)^2$ for ^{108}In

band 5 and $B(E2) < 0.10 (e b)^2$ for ^{110}In band 4, indicating small deformation in both bands. Note that if the side-feeding lifetimes were scaled to be significantly faster than the in-band lifetimes, this would result in an overall increase in the in-band lifetimes and decrease the $B(E2)$ strengths further; thus, the limits quoted here are still valid. The dynamic moments of inertia immediately above the alignments in the two bands are $\mathcal{J}^{(2)} = 80.0\hbar^2 \text{ MeV}^{-1}$ and $71.4\hbar^2 \text{ MeV}^{-1}$, decreasing to $22.6\hbar^2 \text{ MeV}^{-1}$ and $18.1\hbar^2 \text{ MeV}^{-1}$, for ^{108}In band 5 and ^{110}In band 4, respectively. The corresponding lower limits on the $\mathcal{J}^{(2)}/B(E2)$ ratios for the two bands are, therefore, $\mathcal{J}^{(2)}/B(E2) > 251\hbar^2 \text{ MeV}^{-1}$ and $181\hbar^2 \text{ MeV}^{-1} (e b)^{-2}$, both of which are significantly higher than values expected for typical well-deformed rotational bands. For both bands, these $\mathcal{J}^{(2)}/B(E2)$ limits and the similar appearance of the $I'(\omega)$ curves in Fig. 15(a) to those of deformed rotational bands are characteristic properties of AMR bands. On the other hand, the predicted deformations, given in Table VII, correspond to $B(E2)$ values of approximately $0.23 (e b)^2$ for both proposed configurations, which are considerably larger than the estimated values for these bands. If the side feeding into these bands is slow, contrary to the above assumption, this may explain the observed discrepancy; however, this cannot be sufficiently tested in the current analysis.

C. Configuration assignments for other $\Delta I = 1$ bands in $^{108,110}\text{In}$

The dipole band 7 in ^{108}In and bands 7, 8, and 9 in ^{110}In are not as well developed as those discussed in Sec. V A, hence making detailed interpretations more difficult. Qualitative comparisons with theoretical calculations can still be made, however, indicating possible configuration assignments for these bands.

The angular momentum as a function of rotational frequency for all four bands are plotted in Fig. 18, along with ^{110}In band 3, for comparison. Bands 8 and 9 in ^{110}In fall fairly close together in spin to band 3, which suggests that the orbitals involved in each configuration provide a similar amount of angular momentum. This is also apparent from the Routhians of these bands, plotted in Fig. 19(a); the slopes of bands 3, 8, and 9 [$-dE'(\omega)/d\omega = I$] are nearly the same. The apparent similarities among these bands suggest that all are based on three-quasineutron configurations, since one- or five-quasineutron configurations would not so closely match either the spins or energies observed in these bands. The only likely three-quasineutron configurations not yet considered for ^{110}In are $(h_{11/2})^3$ and configurations involving unfavored $g_{7/2}/d_{5/2}$ or $h_{11/2}$ orbitals. Consequently, TAC calculations were performed for the neutron configurations $(h_{11/2})^3$ (EFG), $[(g_{7/2}/d_{5/2})^2 h_{11/2}]$ with unfavored $h_{11/2}$ (ABF), and $[(g_{7/2}/d_{5/2})(h_{11/2})^2]$ with unfavored $g_{7/2}/d_{5/2}$ (BEF). All three calculations were fully optimized with respect to ε_2 and γ (see Table VII). The calculated Routhians for these configurations are plotted in Fig. 19(b) (note that there is an arbitrary energy offset). The approximately equal spacing of the Routhians of bands 3, 8, and 9 is not reproduced, but the relative ordering of the bands compared with the calculations suggests the following correspon-

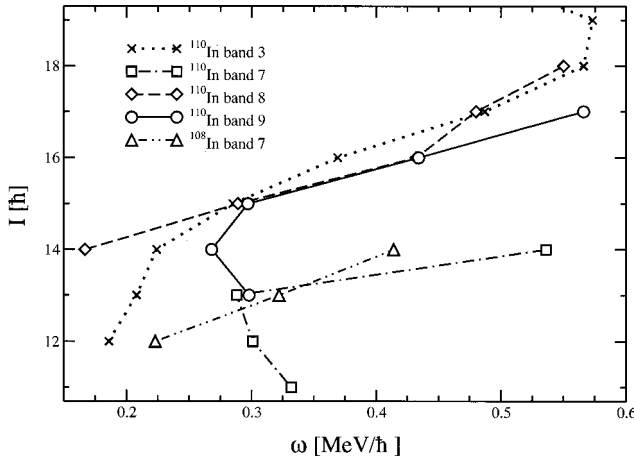


FIG. 18. Angular momentum as a function of rotational frequency for band 7 in ^{108}In and bands 3, 7, 8, and 9 in ^{110}In .

dence: *AEF* with band 3 (as was discussed in Sec. V A 2), *BEF* with band 8, and *EFG* with band 9. These assignments are consistent with the proposed parities for each band. Moreover, as pointed out in Sec. IV B 6, the transitions be-

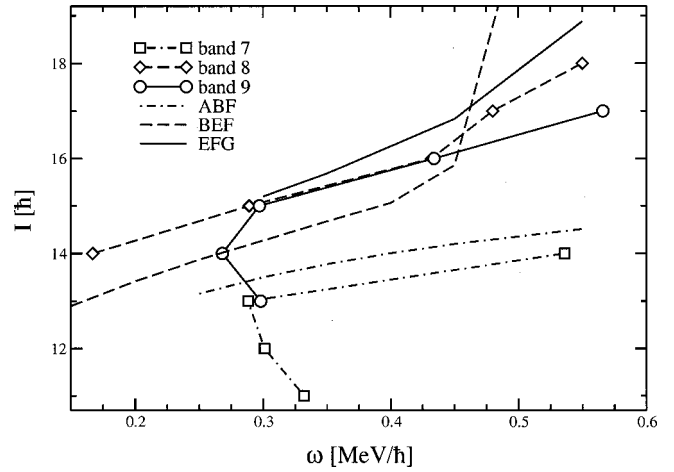


FIG. 20. Angular momentum as a function of rotational frequency for bands 7, 8, and 9 in ^{110}In in comparison with the corresponding TAC calculations for the assigned configurations (see Table VII).

tween bands 3 and 8 are explained by the similarity in the underlying configurations of these bands, which differ only by the favored or unfavored positive-parity neutron orbital. The remaining band 7 and configuration *ABF* also qualitatively agree; their Routhians have shallower slopes than the other Routhians shown in Fig. 19, becoming least yrast of all the bands or configurations considered here at higher rotational frequencies. Thus, band 7 has been assigned the *ABF* configuration.

The calculated $I(\omega)$ for the configurations assigned to bands 7, 8, and 9 in ^{110}In are shown in comparison with the experimental results in Fig. 20. Band 7 and its corresponding configuration *ABF*, plotted with dot-dashed lines, are both lower in spin than the other curves in this figure, as was apparent from the slopes of the Routhians. Both curves have the same slope above the experimental alignment (which is attributed to the *AB* crossing), further supporting this configuration assignment. Band 8 and the *BEF* configuration, plotted with dashed lines, agree to within $1\hbar$ up to the alignment. Both begin to upbend at $\omega > 0.45$ MeV/ \hbar ; this is attributed to the *AD* alignment, since all lower-frequency alignments are blocked. The gradual increase in spin for band 8 at the alignment is not duplicated by the theory. This could indicate that the interaction strength is not properly reproduced for this alignment. It is also possible that neither the 550- or 556-keV transitions associated with band 8 are the extension of this band. The proper (unobserved) extension of band 8 may indicate a significantly sharper alignment. The correspondence between the two remaining curves, for band 9 and configuration *EFG*, plotted with solid lines, is perhaps more questionable than the other two cases. The alignment at $\omega \approx 0.3$ MeV/ \hbar in band 9 has been associated with the *FG* neutron alignment, though the frequency appears to be lower than the expected *FG* alignment frequency at this deformation. The magnitude of the spins in band 9 are approximately reproduced, but the slope of the theoretical curve is too steep. The alignment seen in the calculation at $\omega > 0.45$ MeV/ \hbar is due to the *AB* crossing. (The

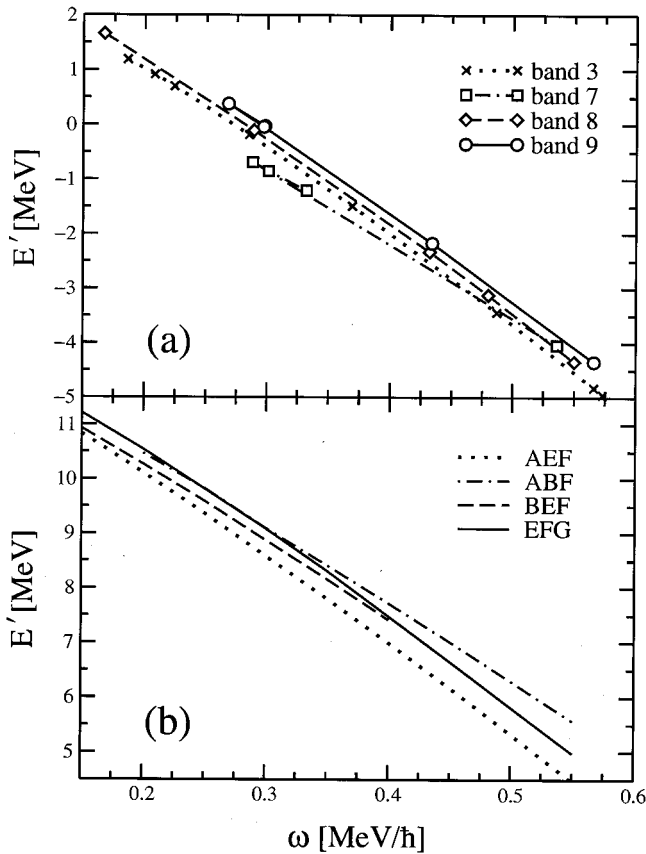


FIG. 19. (a) Experimental Routhians of bands 3, 7, 8, and 9 in ^{110}In . (b) Theoretical Routhians calculated with TAC for select configurations in ^{110}In . Note that there is no energy reference subtracted from the experimental values, as the TAC calculations take core contributions into account. The TAC Routhians have an arbitrary energy offset, but the relative energies are fixed.

presence of the aforementioned *AD* alignment at a lower frequency than this *AB* alignment and the large shift in frequency relative to the *AB* alignment in band 7 is possible when the differences in equilibrium deformation and tilting angle are taken into account.) This alignment is not apparent in the data for band 9, but this is possibly because the band was not observed to high enough spin.

An alternate assignment is possible for bands 8 and 9 by interchanging their assigned configurations. (Although the configurations have opposite parities, bands 8 and 9 have only tentatively assigned parities.) This new configuration assignment is more consistent with the observed alignments in both bands, but does not reproduce the relative order of the Routhians shown in Fig. 19 or explain the crosstalk between bands 3 and 8. Thus, the original assignment is preferred.

Band 7 in ^{108}In is even less developed than the other bands discussed in this section. Considering the close similarities between the observed bands in ^{108}In and ^{110}In discussed so far, it is reasonable to assume that this band may also have a counterpart in ^{110}In . Judging by the magnitude of the spins of band 7 (see Fig. 18), the obvious choice is band 7 of ^{110}In , namely, the *ABF* configuration.

No lifetime measurements were performed for any of the bands discussed in this section. In general, the sequences were too weak and consisted of too few transitions to observe more than one clean, fittable Doppler-shifted transition in each band.

D. Low-spin states in $^{108,110}\text{In}$

Although this work concentrates on the high-spin states in ^{108}In and ^{110}In which exhibit rotational-like properties, a few comments can be made regarding the properties of the low-spin positive-parity states common to both isotopes. Both ^{108}In and ^{110}In have a 7^+ ground state as well as excited states ranging from $I^\pi=7^+$ to 9^+ (in band 6 of ^{108}In) and 7^+ to (11^+) (in band 6 of ^{110}In). The low-spin parts of the ^{108}In and ^{110}In level schemes have been studied by Krasznahorkay *et al.* [31,32]. In those analyses, the experimentally established low-spin states were compared with interacting boson-fermion-fermion model (IBFFM) calculations in an effort to identify underlying configurations. Calculations for both nuclei predicted that the excitation energies of the 2^+ – 7^+ states of the $\pi[(g_{9/2})^{-1}] \otimes \nu[d_{5/2}]$ multiplet form an approximate concave-down parabola at low excitation energy. This is illustrated for ^{108}In in Fig. 21(a).

The 1^+ – 8^+ states of the $\pi[(g_{9/2})^{-1}] \otimes \nu[g_{7/2}]$ multiplet are expected at higher excitation energies. This latter multiplet was shown to exhibit deviations from a parabolic rule in the indium isotopes as the mass decreases from ^{112}In down to ^{106}In (see Ref. [32] and references therein). The concave-down parabola at higher neutron numbers, where the $g_{7/2}$ neutron has holelike character, is predicted to become a W shape, as shown in the left half of Fig. 21(b), and then become a concave-up parabola at lower neutron numbers as the neutron Fermi level occupies $g_{7/2}$ orbitals which have a greater particle-like character. This behavior is sensitive to

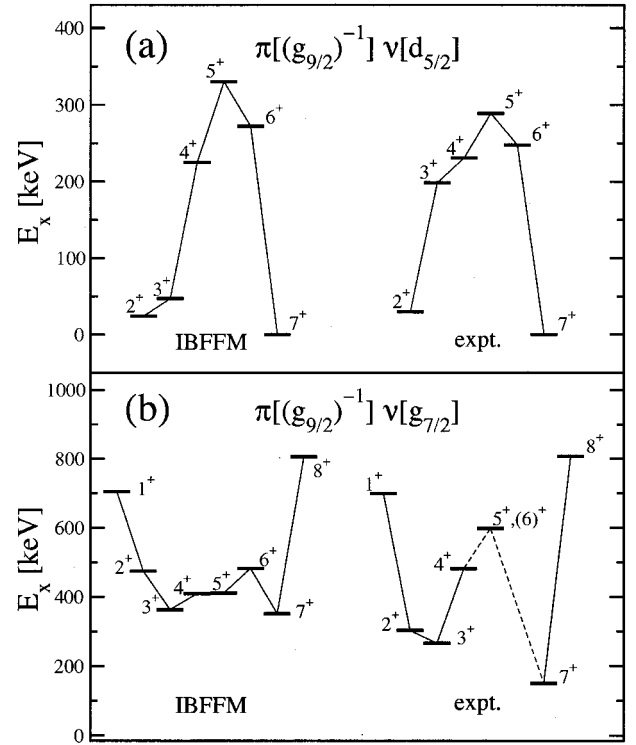


FIG. 21. IBFFM predictions and observed states for the (a) $\pi[(g_{9/2})^{-1}] \otimes \nu[d_{5/2}]$ and (b) $\pi[(g_{9/2})^{-1}] \otimes \nu[g_{7/2}]$ multiplets in ^{108}In . The theoretical values have been estimated from Fig. 9 in Ref. [31]. Experimental data in (a) and for $I \leq 5$ in (b) are also taken from Ref. [31].

the boson-quasineutron interaction strength and Fermi level and is a general characteristic of IBFFM calculations [32,33].

The level scheme deduced for ^{108}In in [31] does not include any experimental counterparts to the predicted 6^+ , 7^+ , or 8^+ states of the $\pi[(g_{9/2})^{-1}] \otimes \nu[g_{7/2}]$ multiplet, leaving the higher-spin portion of the predicted W shape unconfirmed. In the current analysis, excited 7^+ and 8^+ states were observed at 150 and 808 keV, respectively, which could represent two of the missing states of this multiplet. (No 6^+ state was identified in this work. In Ref. [31], the 598-keV state was assigned $I^\pi=5^+$, but a 6^+ assignment was not completely ruled out.) The 7^+ state is about 200 keV lower than the predicted state, but the 8^+ excitation energy is reproduced almost exactly. Associating these and the previously observed 1^+ – 5^+ states with the $\pi[(g_{9/2})^{-1}] \otimes \nu[g_{7/2}]$ configuration confirms the general features of this multiplet in ^{108}In , as indicated in Fig. 21(b). The excited 7^+ and 8^+ states in ^{110}In (at 413 and 714 keV, respectively) confirmed the distorted parabolic shape in that nucleus [32].

The states in band 6 in ^{110}In are seen up to (11^+) . Since the most angular momentum that can be generated solely by the $\pi[(g_{9/2})^{-1}] \otimes \nu[g_{7/2}]$ configuration is $8\hbar$, more particles must be involved in the configuration of band 6. A configuration of $\pi[(g_{9/2})^{-1}] \otimes \nu[(g_{7/2}/d_{5/2})^3]$ is proposed for band 6 in ^{110}In and, analogously, to band 6 in ^{108}In . This assignment is supported by comparison with band 14 in ^{109}Cd [2,28], which is also a short sequence of ~ 650 - to 750 -keV $M1/E2$ transitions. This band in ^{109}Cd was assigned the

$\pi[(g_{9/2})^{-2}] \otimes \nu[g_{7/2}/d_{5/2}]$ configuration at the bandhead [28] and was observed to have a backbend [2], which can be attributed to the alignment of the first allowed pair of positive-parity neutrons (BC), leading to the $\pi[(g_{9/2})^{-2}] \otimes \nu[(g_{7/2}/d_{5/2})^3]$ configuration.² Also, in ^{110}In there is unresolved feeding from band 3 to band 6, which may be similar to the feeding from band 11 to band 14 in ^{109}Cd . (The similarity between ^{109}Cd band 11 and ^{110}In band 3 is discussed in Sec. V A 2.) Band 6 in ^{108}In and ^{110}In , therefore, only differ from the configuration of band 14 in ^{109}Cd by the addition of a $g_{9/2}$ proton. TAC calculations for this band in both of the indium isotopes indicate that stable shears solutions do not exist for this configuration, that is, the cranking axis is not tilted with respect to the principal axes of the nucleus. Part of the explanation for this is likely because the $g_{7/2}/d_{5/2}$ neutrons that are occupied in this configuration are nearing the mid- to high- Ω region of the subshells, which do not couple perpendicularly to the high- Ω proton angular momentum vector. In addition, these positive-parity neutrons contribute less angular momentum than neutrons in $h_{11/2}$ orbitals. High- j orbitals such as the $h_{11/2}$ orbitals are typically required to generate the shears mechanism [11].

The sequence of states labeled band 8 in ^{108}In does not show any regularity. As with the bands discussed above, this band has not been interpreted in the context of the shears mechanism. The strong 1397-keV transition decaying from the 9^+ state directly to the ground state may indicate that this structure involves the coupling of the valence proton hole and neutron of the ^{108}In ground state to the 2^+ state of the ^{108}Sn core; the 1397-keV excitation energy of the 9^+ state is comparable to the ~ 1.2 -MeV excitation energy of the core $^{108}\text{Sn } 2^+$ state.

VI. CONCLUSIONS

The level schemes for both ^{108}In and ^{110}In have been considerably extended. $\Delta I=2$ bands have been observed in ^{110}In for the first time. Reduced transition strengths deduced

²An EF alignment would result in the same configuration as for band 11 in ^{109}Cd , and the alignment frequency is closer to BC than to EF when the tilting angle is taken into account.

from DSAM lifetime measurements in several bands have been compared with TAC predictions. The $B(M1)$ values for the dipole bands exhibit the predicted decrease as a function of spin expected for magnetic-rotational shears bands. Experimental angular momenta have also been found to be in good general agreement with the predicted values for those bands based on configurations including more than two valence nucleons, at least one of which is from the $\nu h_{11/2}$ subshell. For each band in which lifetimes were measured, the ratio $\mathcal{J}^{(2)}/B(E2)$ was found to be over an order of magnitude larger than for well-deformed rotors, suggesting there is a large contribution to the moment of inertia from the closing shears blades. These results indicate that the shears mechanism has a prominent role in the generation of angular momentum in $\Delta I=1$ bands in these isotopes. Additionally, these results also support the interpretation of several of the $\Delta I=2$ bands as antimagnetic-rotational shears bands. Two of the $\Delta I=2$ bands observed to high spins had lifetimes longer than could be measured in these analyses; experiments that are more sensitive to longer lifetimes, such as recoil-distance measurements, are required to quantitatively determine the $B(E2)$ strength in these bands. The majority of the observed sequences in both ^{108}In and ^{110}In have been assigned configurations, although several bands which were not sufficiently developed to make conclusive assignments would benefit from more sensitive high-spin data. In general, the bands in these nuclei have been successfully interpreted using the TAC model. The calculations for the $\Delta I=1$ bands in ^{108}In are in better agreement with the data than are those in ^{110}In . This work extends the knowledge of the role of the shears mechanism in generating angular momentum in nuclei near the $Z=50$ closed shell and suggests that lower-mass isotopes, closer to the $N=50$ closed shell, warrant investigation in this context.

ACKNOWLEDGMENTS

The authors would like to thank A. Lipski for preparing the targets, J. C. Wells for providing the LINESHAPE codes and offering helpful assistance in running them at Stony Brook, and the staffs of the Stony Brook and TASCC accelerator facilities. This work was supported in part by the U.S. NSF under Grant No. 431-0980H, the U.S. DOE under Contract No. DE-FG02-95-ER40934, the NSERC of Canada, AECL Research, and the U.K. EPSRC.

-
- [1] S. Frauendorf, Nucl. Phys. **A557**, 259c (1993).
 - [2] C. J. Chiara *et al.*, Phys. Rev. C **61**, 034318 (2000).
 - [3] N. S. Kelsall *et al.*, Phys. Rev. C **61**, 011301(R) (2000).
 - [4] R. M. Clark *et al.*, Phys. Rev. Lett. **82**, 3220 (1999).
 - [5] A. Gadea *et al.*, Phys. Rev. C **55**, R1 (1997).
 - [6] D. G. Jenkins *et al.*, Phys. Lett. B **428**, 23 (1998).
 - [7] D. G. Jenkins *et al.*, Phys. Rev. C **58**, 2703 (1998).
 - [8] P. Vaska, Ph.D. thesis, State University of New York at Stony Brook, 1997.
 - [9] P. Vaska *et al.*, Phys. Rev. C **57**, 1634 (1998).
 - [10] S. Frauendorf and J. Reif, Nucl. Phys. **A621**, 736 (1997).
 - [11] S. Frauendorf, Rev. Mod. Phys. **73**, 463 (2001).
 - [12] F. Dönau and S. Frauendorf, in *Proceedings of the International Conference on High Angular Momentum Properties of Nuclei, Oak Ridge, 1982*, edited by N. R. Johnson (Harwood, New York, 1983), p. 143.
 - [13] D. G. Jenkins *et al.*, Phys. Rev. Lett. **83**, 500 (1999).
 - [14] R. M. Clark and A. O. Macchiavelli, Annu. Rev. Nucl. Part. Sci. **50**, 1 (2000).
 - [15] A. Bohr and B. Mottelson, *Nuclear Structure* (Benjamin, New York, 1975), Vol. 2.
 - [16] R. M. Clark and A. O. Macchiavelli (private communication).
 - [17] J. Gascon *et al.*, Nucl. Phys. **A513**, 344 (1990), and references therein.

- [18] D. C. Radford, Nucl. Instrum. Methods Phys. Res. A **361**, 297 (1995).
- [19] K. S. Krane, R. M. Steffen, and R. M. Wheeler, Nucl. Data Tables **11**, 351 (1973).
- [20] A. Krämer-Flecken, T. Morek, R. M. Lieder, W. Gast, G. Hebbinghaus, H. M. Jeger, and W. Urban, Nucl. Instrum. Methods Phys. Res. A **275**, 333 (1989).
- [21] J. C. Wells and N. R. Johnson (private communication).
- [22] N. Elias *et al.*, Nucl. Phys. **A351**, 142 (1981).
- [23] E. Andersson, P. Herges, H. V. Klapdor, and I. N. Wischniewski, Phys. Rev. C **24**, 917 (1981).
- [24] R. S. Chakrawarthy, B. S. Nara Singh, and R. G. Pillay, Eur. Phys. J. A **3**, 5 (1998).
- [25] R. Béraud, A. Charvet, R. Duffait, M. Meyer, J. Genevey, J. Tréherne, A. Genoux-Lubain, F. Beck, and T. Byrski, J. Phys. (Paris) Colloq. **41**, C10-159 (1980).
- [26] L. C. Northcliffe and R. F. Schilling, Nucl. Data, Sect. A **7**, 233 (1970).
- [27] F. James and M. Roos, Comput. Phys. Commun. **10**, 343 (1975).
- [28] S. Juutinen *et al.*, Nucl. Phys. **A577**, 727 (1994).
- [29] T. Lönnroth, S. Vajda, O. C. Kistner, and M. H. Rafailovich, Z. Phys. A **317**, 215 (1984).
- [30] J. R. Cooper, R. Krücken, C. W. Beausang, J. R. Novak, A. Dewald, T. Klug, G. Kemper, P. von Brentano, M. P. Carpenter, R. V. F. Janssens, C. J. Lister, and I. Wiedenhöver, Phys. Rev. Lett. **87**, 132503 (2001).
- [31] A. Krasznahorkay, Zs. Dombrádi, J. Timár, T. Fényes, J. Gul-yás, J. Kumpulainen, and E. Verho, Nucl. Phys. **A499**, 453 (1989).
- [32] A. Krasznahorkay, Zs. Dombrádi, J. Timár, Z. Gácsi, T. Kibédi, A. Passoja, R. Julin, J. Kumpulainen, S. Brant, and V. Paar, Nucl. Phys. **A503**, 113 (1989).
- [33] S. Brant and V. Paar, Z. Phys. A **329**, 151 (1988).